Experimental Analysis of a Novel Cooling Material for Large Format Automotive Lithium-Ion Cells

Daniel Worwood [1,*], James Marco [1], Quirin Kellner [1], Elham Hosseinzadeh [1], Ryan McGlen [2], David Mullen [2], Kevin Lynn [2] and David Greenwood [1]

[1] WMG, University of Warwick, Coventry CV4 7AL, UK; James.Marco@warwick.ac.uk (J.M.); Q.Kellner@warwick.ac.uk (Q.K.); E.Hosseinzadeh@warwick.ac.uk (E.H.), d.greenwood@warwick.ac.uk (D.G.)

[2] AAVID Thermacore Europe, Ashington NE63, UK; Ryan.McGlen@aavid.com (R.M.); David.Mullen@aavid.com (D.M.); Kevin.Lynn@aavid.com (K.L.);

* Correspondence: d.worwood@warwick.ac.uk

Abstract: Cooling the surface of large format batteries with solid conductive plates, or fins, has an inherent advantage of reducing the number of liquid seals relative to some mini-channel cold plate designs, as liquid is not passed through the numerous individual plates directly. This may reduce the overall pack leakage risk which is of utmost importance due to safety concerns associated with the possibility of a cell short circuit and thermal runaway event. However, fin cooling comes at a cost of an increased thermal resistance which can lead to higher cell temperatures and a poorer temperature uniformity under aggressive heat generation conditions. In this paper, a novel graphite-based fin material with an in-plane thermal conductivity 5 times greater than aluminium with the same weight is presented for advanced battery cooling. The thermal performance of the fin is benchmarked against conventional copper and aluminium fins in an experimental programme cycling real 53 Ah pouch cells. The results from the extensive experimental testing indicate that the new fin can reduce both the peak measured temperature and surface temperature gradient by up to 8 °C and 5 °C respectively, when compared to aluminium fins under an aggressive electric vehicle duty-cycle.

Keywords: lithium-ion; pouch-cell; battery thermal management; graphite; fin cooling

1. Introduction

In an effort to reduce the global output of greenhouse gas emissions, an increasing number of original equipment manufacturers (OEMs) including Ford [1], Tesla [2] and Volkswagen [3] are employing electrified powertrains within their new and upcoming models of automotive vehicles. A 2017 report by the International Energy Agency (IEA) [4] estimates that as a result of these OEM, together with government initiatives, the global stock of electric vehicles (EV) and plug-in hybrid vehicles (PHEV) may increase from 2 million reported units in 2016 to between 9–20 million units by 2020. Other reports also forecast a significant shift in the global automotive powertrains mix towards electrification, where the combined global market share for EVs, PHEVs and hybrid electric vehicles (HEVs) may exceed 30% by 2030 [5].

Due to their high energy and power density [6], lithium-ion batteries are an attractive choice for the energy storage system contained within EV, PHEV and HEVs, resulting in their widespread adoption by leading automotive OEMs [7]. However, the performance and durability (i.e., ageing rate) of lithium-ion batteries is highly sensitive to their thermal condition [8], which can lead to detrimental effects on the battery if left (thermally) unmanaged [9]. It is commonly reported that an

optimum battery operating temperature may exist for lithium-ion cells, where Pesaran et al. suggested a range of 15–35 °C for LiFePO$_4$-type cathode chemistries to maximise performance whilst limiting high temperature-related ageing effects [10]. Similarly, Tourani et al. [11] suggested a slightly narrower operating window of 20 ± 5 °C for a battery with a Lithium Manganese Oxide (LMO) cathode chemistry, whereas Hosseinzadeh et al. [12] suggested a higher range of 25–35 °C for a large format pouch cell employing Nickel Manganese Cobalt (NMC) cathode chemistry. To ensure that automotive batteries are allowed to remain within their optimum temperature range during operation, in addition to avoiding rapid temperature increases that can lead to a safety critical thermal runaway event [13], battery thermal management systems (BTMS) are, therefore, required [14].

Not only must the BTMS remove or add heat to the battery cell to maintain its optimal operating temperature, it must do so in a manner that inhibits the development of temperatures gradients (both through the cell and between cells) which are known to accelerate the battery ageing rate [15]. Owing to this, it is commonly reported [16–20] that the magnitude of the gradient should not exceed circa 5 °C. The design of the BTMS must also be conducive towards a low weight and a high compactness, given the constraints imposed by automotive OEMs [21]. A successful BTMS must, therefore, satisfy the temperature constraints on the battery without significantly reducing the overall pack level gravimetric and volumetric energy density.

Large format pouch-type lithium-ion batteries are a common choice as the battery form factor within automotive energy storage systems [22] and have received growing attention towards their thermal management method. Forced air cooling [23] across the cell body benefits from its simplistic (low cost) and light-weight design, given that weighty metallic cold plates and secondary liquid-to-air heat exchangers are not required [24]. However, the poor heat capacity of air (circa 1006 J·kg^{-1}·K^{-1} relative to circa 3320 J·kg^{-1}·K^{-1} for a typical water glycol mixture [25]) makes it difficult to achieve the required heat removal without worsening its temperature uniformity [8], which is particularly problematic for cells with a long flow path and/or high heat generation rate [25]. Packing the air channels with aluminium foam [26] or attaching bespoke heat sinks to the battery surface as in Reference [27] can extend the use of air cooling under more intensive current loads by mitigating these issues. However, these specific designs require a large cell-to-cell spacing (to accommodate the air channel and/or cooling plate), which can be detrimental to the volumetric energy density of the cell stack. An inordinate amount of parasitic cooling power is also generally required for air-cooled systems relative to liquid-cooled systems to satisfy thermal constraints as the battery heat load increases [28]. This may explain why an increasing number of OEMs such as Tesla [29] and Chevrolet [30] are opting for indirect liquid cooling in their respective models of EVs and PHEVs.

Common liquid-cooled methods for pouch or prismatic cells involve attaching mini-channel cold plates to the battery surface. Examples of these approaches can be found in References [31–33]. As the heat transfer medium is contained within the cold plate channels, the use of conductive mediums with superior heat transfer properties can be used. Chen et al. [34] demonstrated through a simulation that indirect plate cooling pouch cells with a water–glycol mixture offered greater surface temperature uniformity and a lower cell temperature rise than direct cooling with a nonconductive mineral oil, provided that the plate flowrate exceeded circa 0.75 g s^{-1}. However, as highlighted by Kim and Pesaran [25], care must be taken with indirect cooling methods to ensure that the added thermal resistance between the cell surface and heat transfer medium does not offset the heat transfer benefit from using conductive fluids. The risk of leakage is also greater in these systems that use electrically conductive fluids given the severity of a thermal runaway event associated with a cell short circuit [35].

Other developing methods of indirect liquid cooling involve placing conductive sheets between the battery cells (commonly termed fin cooling or extended surface cooling) where the heat from the cell surface is transferred to an external location to be further dissipated [34]. These approaches have the advantage of simplifying the duct and tubing arrangement, given that the fluid is not passed across the large bodies of all the individual cells. Fewer manifold connections and/or seals may, therefore, be present relative to mini-channel cold plates, where the external liquid-cooled location

may also be positioned in a safer area away from the cell compartment to improve the overall safety of the battery pack [36]. Basu et al. [36] presented a novel extended surface BTMS design for cylindrical cells using aluminium conduction elements to transfer heat to two side cold plates. From their simulations, they concluded that the design could efficiently limit the maximum cell temperature rise across a string of 5 cells to within circa 7 °C at the end of a 2.7 C discharge, whilst operating with low liquid velocities in the side cold plates (0.01 m s^{-1}). Hosseinzadeh et al. [37], however, concluded that placing aluminium fins between large format pouch cells may be a poor thermal management choice under more aggressive heat generation conditions (3 C and 5 C). Specifically, for a simulated 40 Ah pouch cell at the end of a 3 C discharge subject to single-edge aluminium fin cooling, an extreme volumetric temperature gradient of 22.9 °C was predicted through the battery. Increasing the sandwich fin thickness from 1.5 mm to 5 mm could lower the gradient to 11.9 °C but may be impractical due to the added weight and volume penalty. Chen et al. [34] further demonstrated that single-edge fin cooling large format batteries with aluminium fins may add excessive weight to the cell (39%) relative to mini-channel cold plate cooling (7%) for a fixed volume penalty. Evidently, there is scope within the literature to improve the thermal efficiency of fin cooling when applied to large format batteries.

In this paper, the thermal performance of a novel super conductive, light-weight fin material is investigated to advance the use of fin cooling for large format pouch type batteries. The paper is structured as follows. Section 2 describes the fin materials used and outlines the design and assembly procedure of the test rig used to experimentally measure the thermal performance of the fin materials. The experimental testing procedure, together with the drive cycle profiles used to electrically load the cells is also discussed in Section 2. In Section 3, the experimental temperature results from the test rig for the highly conductive fins are compared against conventional copper and aluminium fins under a wide range of electrical loading conditions that cover standard EV, PHEV and high performance EV race conditions. Further, a discussion on weight and volume metrics for the different fin materials is included. Further work and the conclusions are contained in Section 4 and Section 5, respectively.

2. Materials and Methods

2.1. Test Rig Design

The test rig is designed to provide independent fin cooling on the front and back surfaces of three large format pouch batteries (53 Ah with a graphite anode and NMC cathode manufactured by XALT Energy [38]). The dimensions of the XALT 53 Ah pouch cells are shown in Figure 1.
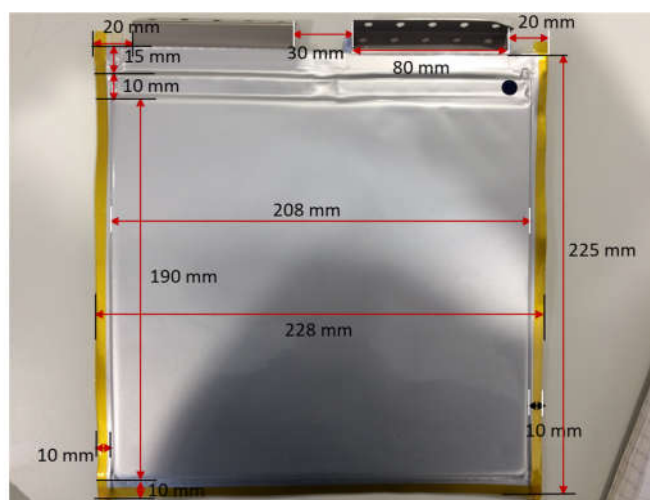

Figure 1. The measured dimensions of the XALT 53 Ah pouch cell.

The cells contained within the rig are separated by layers of insulating material, which act as a support structure for the cells and cooling fins in addition to isolating the cells from one another to achieve independent samples. The test rig is arranged to provide an insulated boundary on the surface of the fin not in contact with the cell to be more reflective of stack level cooling with a fin twice as thick. Figure 2a displays a schematic of the fin-cooled concept on the half-cell level demonstrating the symmetry plane, where Figure 2b shows a top-down view of the test rig design on the stack level. One edge of each of the cooling fins is bent to provide 25 mm of contact length onto an external cold plate, which is used to dissipate the heat from the fin. A detailed discussion on the test rig assembly procedure and design rationale is contained in Section 2.3.
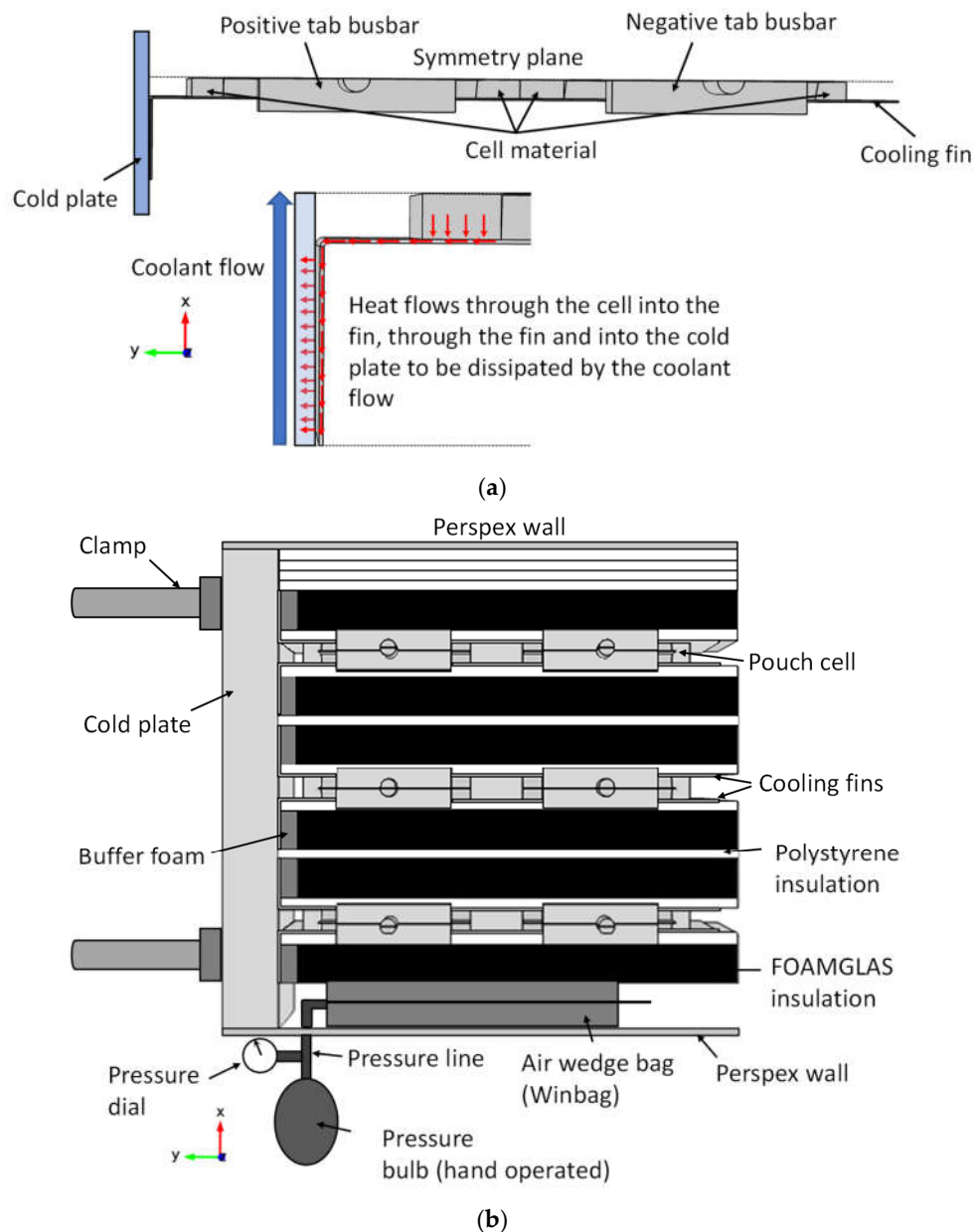

(**a**)

(**b**)

Figure 2. A schematic of the test rig fin-cooled concept and design with (**a**) a half-cell-level displaying the symmetry plane and (**b**) a stack-level design (top down view).

2.2. Fin Materials and Thermocouple Placement

The primary fin material under investigation is comprised of an annealed pyrolytic graphite (APG) core, which is encapsulated within an aluminium foil skin layer. The general manufacturing steps of the APG-based fin first involves manufacturing Pyrolytic graphite (PG) using a chemical vapour deposition process (CVD) through the pyrolysis of natural gas. The PG is deposited on a suitable substrate within a vacuum, at a temperature between 1750–2250 °C [39]. The APG is then formed by annealing the PG at elevated temperatures of up to 3600 °C [40]. The formed APG is then cut to size and bonded to the skin layer.

The skin layer provides mechanical support and protection for the APG core which is fragile in nature [40]. The formed composite sleeve is termed the "k-core" by the industrial partner. The annealing process enables the APG core insert to have a very high thermal conductivity along the axial plane of APG, where conductivity values as high as 1700 W m^{-1} K^{-1} are achievable at 25 °C depending on the manufacturing process [41]. However, heat conducted perpendicular to the APG layers is poor and of the order of 10 W.m^{-1}.K^{-1}. In applications that require a thick k-core insert, thermal vias of conductive metal can be inserted to channel the flow of heat into the APG, improving the effective thermal conductance of the finished part [42]. The k-core technology is identified as a promising material for use in a fin-based BTMS due to its much higher thermal conductance relative to aluminium and lower density (2260 kg m^{-3} for APG vs. 2700 kg. m^{-3} for aluminium [41]) that offers the potential for weight reduction and superior thermal performance. The effective axial thermal conductivity of the composite k-core fins in this work are specified as 1100 W m^{-1} K^{-1} (provided by the industrial partner), which is circa 5 times greater than aluminium. This value is comparable to similar k-core products manufactured by Thermacore [42].

Figure 3a demonstrates the APG core contained within the sleeve, together with the aluminium skin layer encapsulant. A side-by-side comparison between the k-core fin and reference aluminium fin is also shown in Figure 3b. Due to the fragility of the APG, the k-core fin requires a minimum bend radius of 7.5 mm to form the contact length onto the cold plate. The bend radius for the k-core samples is achieved by welding an iron rod (15 mm in diameter) onto a flat metal plate such that the weld joint forms a flat surface. The k-core fin is carefully formed over the rod to achieve the flat 25 mm of contact following the completion of the bend. For the baseline copper and aluminium sheets, a perpendicular bend is achieved with a hand-operated sheet metal break, again enabling 25 mm of flat contact length.

The dimensions and weight of the fin samples are shown in Table 1. The laminate foil on the k-core fin gives a boundary of 5 mm around the APG core, which is neglected in the height and length dimensions shown for the fin body and contact length sections. For measuring and weighing, the average values over the 6 samples are taken. A micrometer with an accuracy of 0.01 mm is used to measure the thickness of the fin sheets, where 3 measurements are taken for each sample (two on the fin body and one on the bent contact edge). The average over all measurements and samples is taken to represent the fin thickness. The APG core thickness and aluminium skin is also measured separately, with values of 0.52 ± 0.01 mm for the APG core and 0.08 ± 0.01 mm for the skin layer.
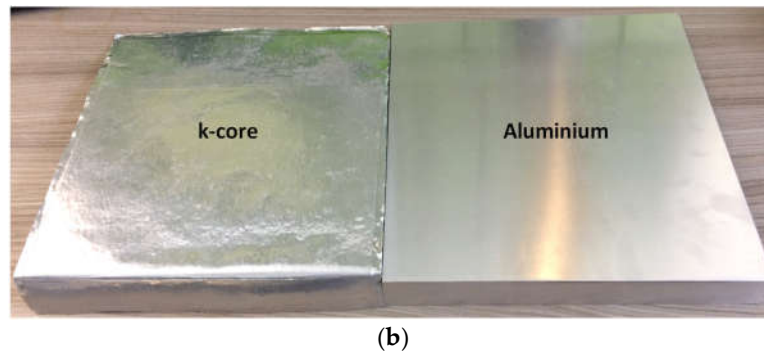

(**a**)

(**b**)

Figure 3. The fin materials used with (**a**) k-core fin with revealed the annealed pyrolytic graphite (APG) core and skin layer and (**b**) a side-by-side comparison of the k-core fin and aluminium fin.

Table 1. The measured fin properties of the experimental samples.

Fin Material	Fin Body Dimensions			Fin Contact Length Dimensions			Fin Weight (g)
	Height (mm)	Length (mm)	Thickness (mm)	Height (mm)	Length (mm)	Thickness (mm)	
Copper	220 ± 1	235 ± 1	0.52 ± 0.01	220 ± 1	25 ± 1	0.52 ± 0.01	258 ± 1
Aluminium	220 ± 1	235 ± 1	0.50 ± 0.01	220 ± 1	25 ± 1	0.50 ± 0.01	74 ± 1
k-core	210 ± 1	220 ± 1	0.68 ± 0.01	210 ± 1	25 ± 1	0.68 ± 0.01	74 ± 1

To track the temperature evolution of the fin in contact with the cell during operation, T-type thermocouples are located across the fin surface. The thermocouples are 1 m in length where the two conductor wires are point welded. giving an exposed junction diameter of circa 0.3 mm. The thermocouples have a temperature range of −200 °C to +350 °C which is deemed suitable for the experiment. A direct thermocouple attachment onto the cell surface is not attempted due to the creation of air gaps which would hamper the heat transfer into the fin, in addition to safety concerns of the pinpoint thermocouples piercing the pouch cell when under stack compression. Figure 4a highlights the 15 thermocouple (TC) arrangement adopted for the k-core fin, and Figure 4b is the arrangement adopted for the copper and aluminium reference case fins. With reference to Section 2.3.3, this thermocouple placement is only present on the front fins for each cell due to limitations in the number of measuring channels. On the back fins, 3 thermocouples are placed at locations 5, 7 and 9 to check for parity between readings on both fins. The rationale for the location of the thermocouples is to provide as wide a coverage as practical to better capture the temperature evolution across the fin surface. An effort is made to identify the maximum fin temperature which is expected to be at TC5 as it is furthest from the cooling source and the maximum fin temperature gradient which is expected to be TC5–TC9. Knowledge of these metrics is important for the design of the thermal management system which is discussed further in Section 3.2. The thermocouples are fixed to the fin surface with adhesive Kapton tape (in the manner as shown in Figure 4a) to minimise any displacement during the assembly process.
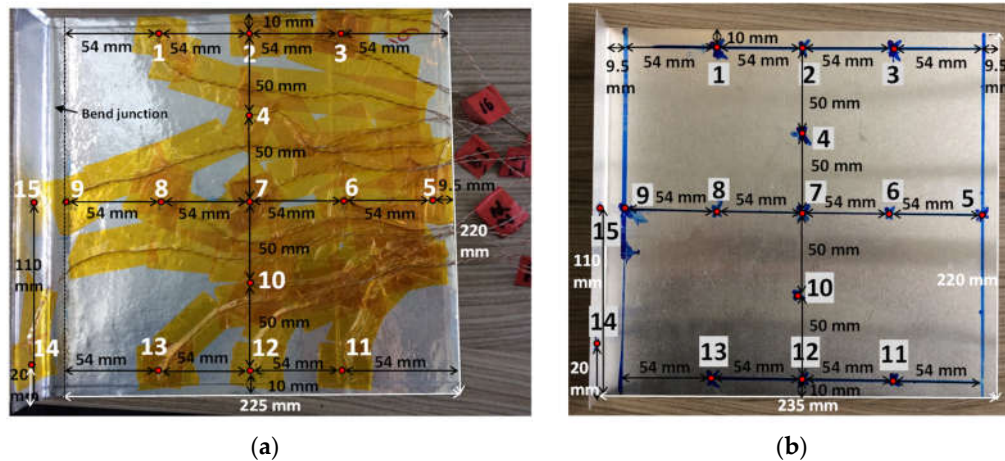
(**a**)   (**b**)

Figure 4. The thermocouple locations for (**a**) the front k-core fin and (**b**) the front aluminium and copper fins (aluminium fin shown in the image).

2.3. Test Rig Assembly Procedure

2.3.1. Stage 1—Insertion of the First Insulation Layers and Metallic Cooling Fin

The test rig shell consists of multiple Perspex walls attached together with threaded screws. During the first stage of assembly, one of the outer walls is removed to enable top-down access to the rig. The first layer of insulation material is added, which consists of four 5-mm-thick polystyrene sheets placed in contact with the test rig outer wall. Four sheets are chosen to provide an increased compactness.

Following the addition of the polystyrene sheets, a 20-mm-thick slab of FOAMGLAS (Pittsburgh Corning, Pittsburgh, PA, USA) is added as the second distinct layer. The FOAMGLAS material is highly insulative in nature with a thermal conductivity of 0.046 W m^{-1} K^{-1} at 40 °C [43]. A further polystyrene sheet is placed in between the FOAMGLAS and subsequently stacked metallic cooling fin. This is to protect the fin from the abrasive nature of the FOAMGLAS which is comprised of sintered glass particles. In between the bent edges of the fins and FOAMGLAS, a compressible buffer foam layer is added (10 mm thick and 20 mm in width) to protect the thermocouples along the fin edge from the FOAMGLAS when the rig is pressurised.

Busbar blocks are attached to the roof of the test rig. The busbars are comprised of two brass blocks, where one block contains an M8 screw thread. In this block, an M8 brass screw is welded into the thread to ensure the creation of minimal resistance. The protruding length of the screw from the busbar is 5 cm in length.

Figure 5 displays the completed Stage 1 arrangement following the addition of the metallic cooling fin (k-core fin shown in this instance). The cooling fin is slotted on top of the outer polystyrene sheet, with the bent fin edge supported by the strip of buffer foam.
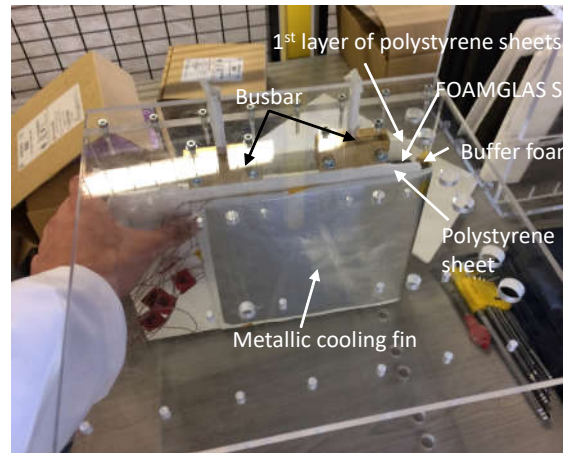
Figure 5. The addition of the first fin insert.

2.3.2. Stage 2—Insertion of the First Cell, Back Fin and Partitioning Material

With reference to Figure 6a–c, following placement of the first fin (front fin), the first cell is added. The remaining fin (back fin) is placed in contact with the other surface of the cell followed by a 5-mm polystyrene sheet and subsequent 20-mm-thick FOAMGLASS slab. The cell tabs are positioned within one busbar block, with the second block added on top and clamped to the other block using screws. The cell is positioned such that the aluminium positive tab of the cell is located near the cooling edge of the fin, with the negative copper tab located at the rear of the test rig furthest from the cooling source. This stacking arrangement is repeated for the remaining two cells.
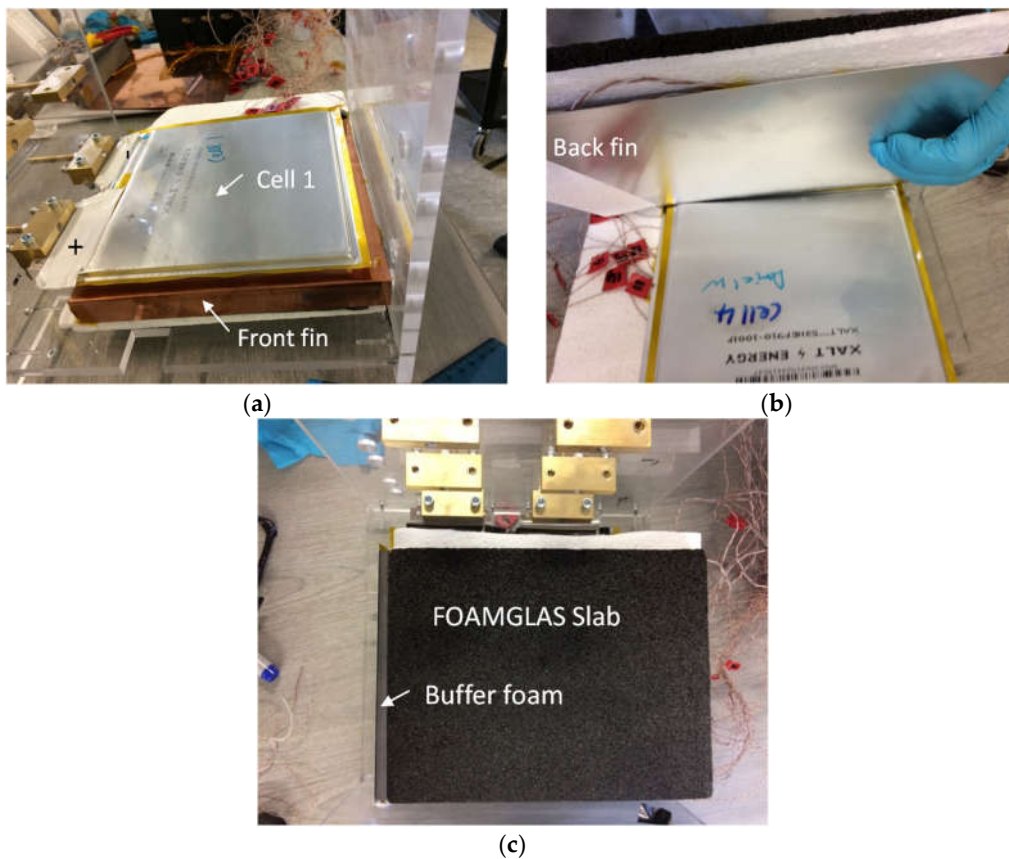

(**a**)

(**b**)

(**c**)

Figure 6. Stage 2 of the assembly with (**a**) the addition of the first cell, (**b**) the addition of the first back fin and (**c**) the addition of the partitioning insulation material.

2.3.3. Stage 3—Insertion of Remaining Cells, Side Air Wedge Bag and Cold Plate

With reference to Figure 7a, upon completion of stacking with the remaining cells, an air wedge bag (winbag) is added in between the outer FOAMGLAS slab and test rig wall to apply pressure on the stack. The side pressure compresses the stack to increase thermal contact between the cooling fin and cell surfaces. The air wedge bag is hand operated, where the applied pressure is controlled via the use of the pressure dial. The pressure is applied manually until the dial reads 0.2 bar, which is the maximum pressure allowed until the test rig wall begins to bulge. This pressure is used for all experiments to ensure parity between tests.

On the side walls of the test rig, the sections are machine cut to accommodate the inlet and outlet hoses of the cold plate, which is placed into the front face of the test rig. An additional cut is also made on one side to accommodate the air wedge bag pressure line. The location of the cold plate is viewable in Figure 7b. A back Perspex panel is added to the rear of the rig to provide a rigid surface for the pressure to be applied. A buffer foam is added onto the rear of the FOAMGLAS slabs in between the back Perspex panel to further distribute the pressure equally between the slabs. Four clamps (two shown in Figure 7b,c) are tightened to push the rear edges of the FOAMGLAS onto the front of the stack, in turn providing a pressurised contact of the fin edge onto the cold plate to minimise thermal contact resistances.

(a)

(b)

(c)

Figure 7. Stage 3 of the assembly with (**a**) a completed stacking arrangement (with k-core fins), (**b**) the addition of the front cold plate and (**c**) the side view of the test rig showing the air bag position.

2.3.4. Stage 4—Electrical and Thermal Interconnectors

For testing, the rig is transferred to a climate chamber (VT 3050). The inlet and outlets of the external cold plate are connected to a LAUDA Thermostat unit, where a flowrate of 10 L.min^{-1} of a water–glycol mixture is pumped through at a regulated set-point temperature of 25 °C.

The electrical load cables on the cell are connected to the protruding screws from the cell busbars. A total of 4 cables per busbar is used to accommodate peak currents of up to 400 A. Figure 8a displays the complete arrangement of the test rig within the climate chamber. The insulation (plastic wool) is added to the exposed portions of the test rig where large air gaps exist to limit the effect of convective cooling from the climate chamber ambient. The data logger tracking the thermocouple temperature (Hioki 8423 Memory HiLOGGER with 8948 Voltage/Temp units) is also viewable. The data logger has a sampling rate of 1 s and is set to continuous monitoring mode.

The four clamps are distributed symmetrically near the top and bottom portions of the cold plate to provide a uniform pressure onto the fin edges. Figure 8b displays an exploded view of the fin contact onto the cold plate.
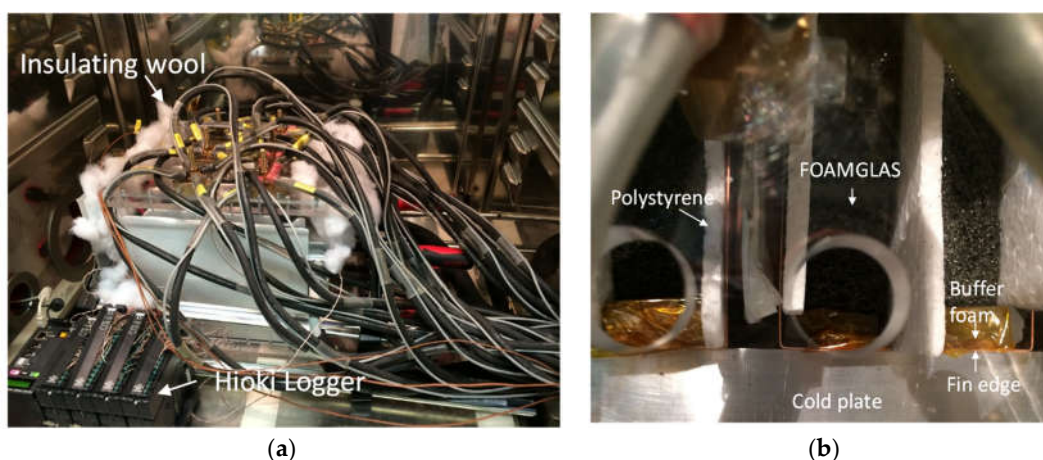

(a) (b)

Figure 8. Stage 4 of the assembly with (**a**) a fully assembled test rig within the climate chamber with thermal and electrical interconnectors in place and (**b**) an exploded view of the contact between the fin edge and external cold plate.

2.4. Testing Procedure

To thermally test the performance of the different fin materials, 6 of the unaged 53 Ah cells with a nominal voltage of 3.7 V are subject to 3 loops of a PHEV World Wide Harmonised Light Vehicle Test Procedure (WLTP) Class 3 duty cycle (1800 s per loop) and a separate high-performance race duty cycle, which is viewable in Figure 9a,b (negative current denotes discharge and positive current charge). The starting cell state-of-charges (SOC) for the WLTP and race cycle are 100% and 95%, respectively. Standard 1 C, 2 C and 3 C full discharges (from 100–0% SOC) are also analysed to provide further thermal comparisons.

The PHEV WLTP Class 3 Cycle has been used previously in Reference [44] and has been extended to accommodate the use of 53 Ah cells in this study. This results in a 16 kWh PHEV comprising of 82 53 Ah cells. The derivation of the race cycle is beyond the scope of this paper and is discussed further [44,45]

Prior to the initiation of the test current profiles into the cycler software, the thermal chamber is left to reach its set point temperature of 25 °C. The Hioki logger is left to track the temperature readings from the thermocouples continuously at a 1 s sampling rate. The software then initiates the current profile into each of the 3 cells within the test rig to commence the experiment.

Following the completion of the current profile, the cells are left to cool for 1 h before being charged back to 100% SOC using a constant current constant voltage charging procedure. This involves holding the charging current at 53 A until the cell voltage reaches 4.2 V, after which the

charging voltage is held at 4.2 V until the trickle current reaches 2.65 A (C/20). Following charging, the cells are rested until thermal equilibrium with the cooling ambient is reached before the next current profile is applied.

Following the completion of the testing across all duty cycles with cells 1, 2 and 3, the rig is disassembled and the cells switched for 3 other unaged cells (cell 1 → cell 4, cell 2 → cell 5 and cell 3 → cell 6). This is performed to increase the number of cell samples for the experiment.
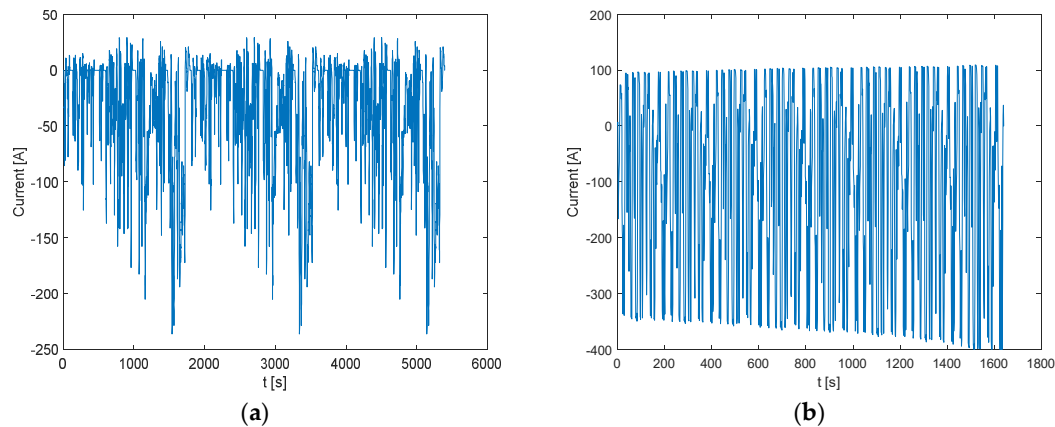

Figure 9. The drive cycle current profiles used for the experiment with (**a**) the WLTP Class 3 cycle and (**b**) Race cycle.

3. Results and Discussion

In this section, the measured thermal outputs obtained from the test rig are discussed in detail for each tested electrical loading condition and fin material type.

Due to issues with the cycler equipment failing to reinitiate the testing between some cycle runs, the full set of 6-cell readings is not obtainable for all analysed electrical loading conditions. Table 2 displays the number of successful cell samples obtained for each fin material type and each duty cycle.

Table 2. The number of experimental cell samples obtained for each analysed electrical loading condition and fin material type.

Test Case	Fin Material					
	Aluminium		Copper		k-Core	
	No. Cell Samples	Cell Number	No. Cell Samples	Cell Number	No. Cell Samples	Cell Number
Race	4	1 *, 2, 3, 4	5	1, 3, 4, 5, 6	5	1, 3, 4, 5, 6
3 C	5	1 *, 2, 3, 4, 5	6	1, 2, 3, 4, 5, 6	6	1, 2, 3, 4, 5, 6
2 C	5	1 *, 2, 3, 4, 5	6	1, 2, 3, 4, 5, 6	1	6
WLTP Class 3	1	4	2	1, 4	2	4, 5
1 C	2	3, 4	4	1, 3, 4, 5	4	3, 4, 5, 6,

* Cell 1 was damaged during disassembly prior to the aluminium fin tests; therefore, it was replaced with a new cell termed Cell 1.

Given that thermocouple readings are present at locations TC5 and TC9 on both the front and back fins, it is important to first test whether there exists any significant statistical evidence that a difference exists between the readings from both the front and back fins. Such a difference may suggest that the test rig has not been set up correctly to achieve the desired symmetry along the cell central plane, as shown previously in Figure 2a. To test whether a difference exists between the front and back fin measurements, a paired student t-test is conducted on the measurements obtained at the end of the 3 C discharge, which is chosen given that this test case has the greatest number of cell

samples for all fin material types. At the $\alpha = 0.05$ level, the t-test accepts the null hypothesis that the difference between the readings is zero; therefore, there is statistical evidence supporting that the rig has been assembled (for cells 1, 2 and 3) and reassembled (for cells 4, 5 and 6) in a manner to achieve the desired symmetry condition.

3.1. Thermal Contact Resistance

Surface asperities present on the pouch cell and fin material result in multiple heat transfer modes across the interface between the two surfaces. These include the conduction between the points at which both surfaces are in contact, through conduction in the gas (in this instance air) that fills the gaps between the surfaces, through convection of air in the gaps and through radiation across the gaps [46]. These heat transfer modes are typically characterised via a thermal contact resistance, where methods to reduce this resistance may include the application of pressure to increase the solid–solid contact area and/or the addition of a thermal interface material to improve gap heat transfer.

In this study, it has been chosen to avoid the use of a thermal interface material and rely on the applied pressure achieved within the test rig via the use of the air bag. To test whether there exists a large contact resistance that would result in a noticeable temperature drop between the cell surface and the measured thermocouple location on the fin surface, an additional thermocouple (termed T_{edge}) is attached with Kapton tape on the accessible edge of the cell during testing with the aluminium fins. The location of the thermocouple on the side of the cell is shown in Figure 10a, which shares the same y-coordinate position as the location of TC5.
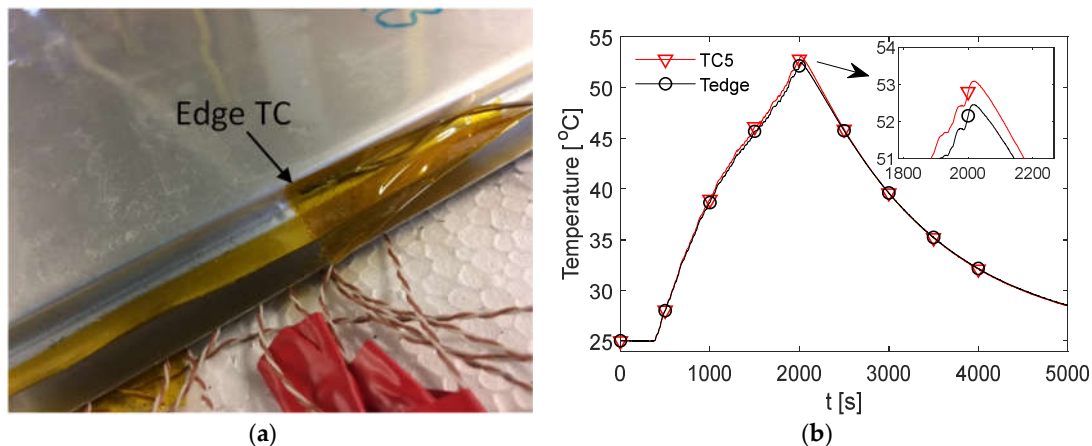

(**a**)   (**b**)

Figure 10. (**a**) The position of the cell edge thermocouple and (**b**) a comparison between the cell edge temperature and TC5 with aluminium fin cooling under the race duty cycle for Cell 3.

A comparison between T_{edge} and TC5 on the back fin (which is closest to the thermocouple location) during the race duty cycle for Cell 3 is shown in Figure 10b. Here, it is observed that there is a maximum difference of 0.64 °C between the two measurements at the end of the cycle, whereby T_{edge} is slightly cooler than TC5. This is not as expected given that there would exist a temperature drop across the interface and through the thickness of the fin. This may be explained due to the edge of the cell being exposed to the ambient air present in the spacing at the rear of the test rig and, therefore, experiences a cooling effect that is not present at TC5 which is sandwiched between the cell and the insulating polystyrene material. It is also possible that the difference is attributed to variability in the thermocouples, given that the value is lower than 1 °C.

The thermal resistance for conduction through the thickness of the fin under steady-state conditions may be expressed as [46]

$$R = \frac{x_f}{A.\,k_x} \tag{1}$$

where R is the thermal resistance (K W^{-1}), x_f is the thickness of the fin (m), A is the cross-sectional area perpendicular to the heat flow (m^2) and k_x is the thermal conductivity of the fin in the direction of the heat flow (in this case, in the x-direction with reference to the coordinate scale in Figure 2) (W m^{-1} K^{-1}). The calculated R value for the k-core fin when taking k_x as 10 W m^{-1} K^{-1}, A as 0.0395 m^2 and x_f as 0.52 mm for the APG core (neglecting the skin layer presence) results in a value of 0.0013 K W^{-1}. The battery heat generation rate assuming only irreversible components is expressed via [47]

$$Q = I^2 R_\eta \tag{2}$$

where Q is the battery heat generation rate (W), I is the cell current (A) and R_η is the cell overpotential resistance (Ω). Assuming a static value of 1.33 mΩ for R_η based on the quoted resistance value given by the cell manufacturer at 50% cell SOC [38], the average value for Q across the race duty cycle is calculated as 49.2 W. Assuming a worst case scenario that 24.6 W is transferred into each fin upon reaching a quasi-steady-state, the temperature drop across the thickness of the fin is calculated as 0.03 °C, which may be assumed negligible. The thermal contact resistance is defined as [46]

$$R_{tc} = \frac{\left(T_{cell} - T_f\right)}{q} \tag{3}$$

where R_{tc} is the thermal contact resistance (m^2 K W^{-1}), T_{cell} is the cell surface temperature (K), T_f is the fin surface temperature (in contact with the cell surface) and q is the heat flux (W m^{-2}). Given the surface area of the cell body is 0.0395 m^2, the steady-state heat flux again assuming 24.6 W is 622.8 W.m^{-2}. For a 1 °C drop to exist between the cell and fin surface, an R_{tc} value of 16.1 × 10 °C^{-4} m^2 K W^{-1} is calculated. For comparison, Xia et al. [48] reported a value of R_{tc} on the order of 1 × 10^{-4} m^2 K W^{-1} for a typical indirect liquid-cooled system. Therefore, poor contact between the fin and pouch cell surface would have to be present for the temperature gradient across the junction to exceed 1 °C.

The results from this analysis, together with the experimental data from Figure 10b do not support a temperature drop between the cell and measured fin surface exceeding 1 °C. It may, therefore, be a reasonable assumption to assume that the measured fin surface temperature approximates the temperature on the cell surface for a given yz coordinate under even the most aggressive of testing scenarios. Ultimately, further testing would be required to determine the exact value of R_{tc} for this system.

For a practical application within a real vehicle system, the use of a thermal interface material such as double-sided adhesive tape (as employed in Reference [20]) may be required if sufficient stack pressure cannot be applied. One potential advantage of the k-core material over the conventional copper and aluminium materials in this regard is from its additional flexibility, which may allow it to better conform to the pouch cell surface to further reduce the thermal contact resistance and/or to remove the need for a thermal interface material. Further work may wish to seek the relationship between the applied stack pressure and the thermal contact resistance for the different fin materials.

3.2. Identification of the Fin Hot Spot and Maximum Temperature Gradient

The maximum fin temperature $(T_{max,f})$ and maximum fin temperature gradient $(\Delta T_{max,f})$ are important parameters to gauge the thermal performance of the thermal management system. It is desirable to reduce $\Delta T_{max,f}$ to ensure that the cell operates at a more uniform temperature, whereas a lower $T_{max,f}$ is desirable to reduce the rate of high-temperature-related ageing mechanisms for the cell. Controlling $T_{max,f}$ is also imperative to ensure that upper temperature thresholds for the cell are not exceeded, thus reducing the risk of the cell entering a thermal runaway event.

Figure 11 demonstrates the temperature measurements obtained across the front fin sample of Cell 4 for each of the analysed fin materials during the race duty cycle. For the k-core fin (Figure 11a), it is observed that TC5 provides the hottest measurement followed closely by TC11. This is to be expected as TC5 is the furthest measured location from the cooled edge of the fin. It is also observed that TC11 is hotter than TC3, which implies that the cell is experiencing a degree of cooling on the

tabs leading to hotter temperatures towards the base of the fin for a given position along the *y*-axis. Cooling at the tabs may be caused due to the brass busbar blocks providing a large thermal mass, where any accumulated heat is further conducted through the busbar and along the protruding brass screw to be dissipated to the ambient via the active air circulation within the climate chamber. This is consistent with the observations of Grandjean et al. [22], who applied a similar mechanism of achieving an electrical connection to the tabs of large format pouch cells and witnessed a cooling effect on the tabs during aggressive electrical loading conditions (5 C in their case).

(**a**)

(**b**)

(**c**)
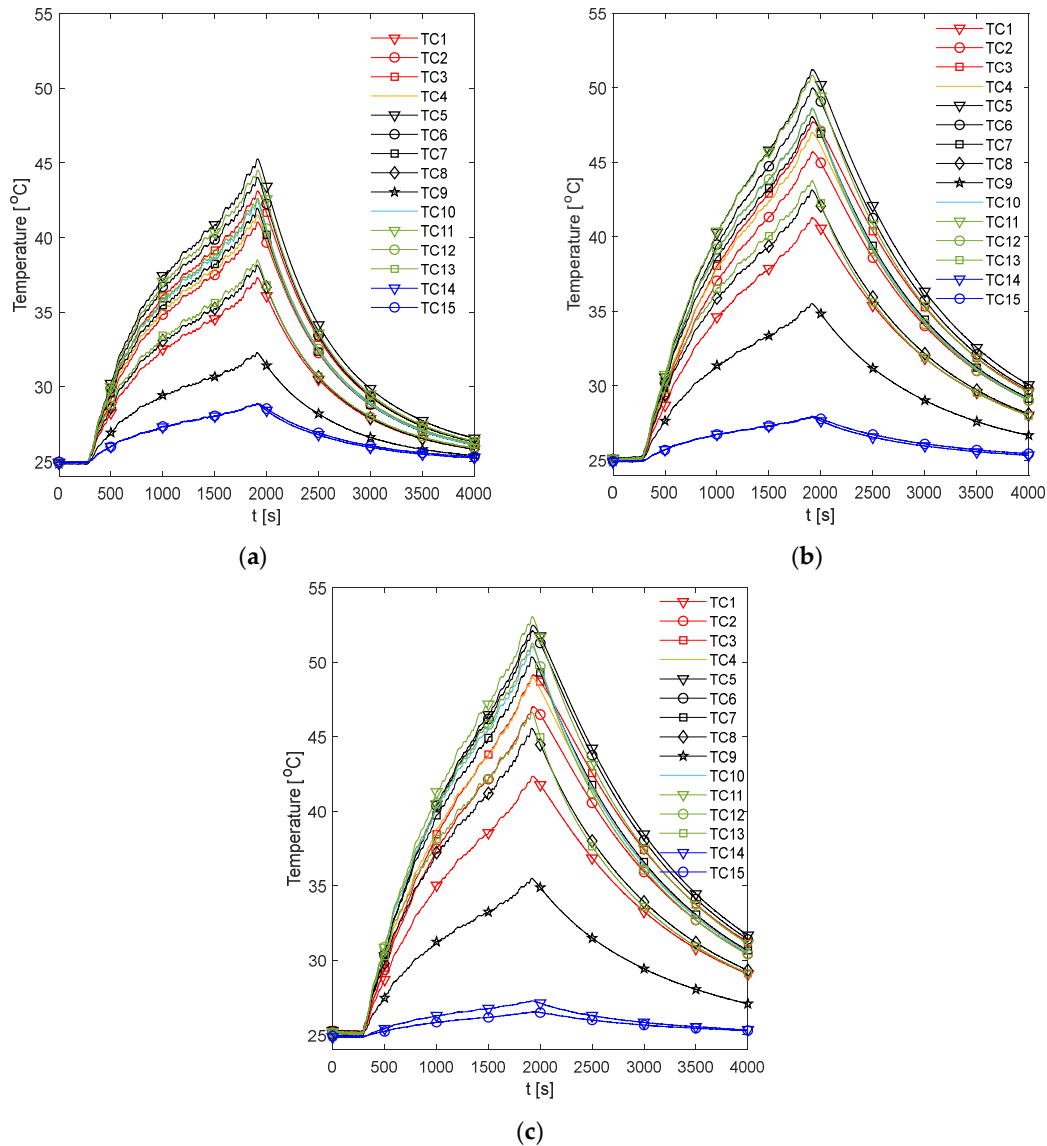
Figure 11. The thermocouple measurements across the front fin for Cell 4 during the race duty cycle with (**a**) k-core fin cooling, (**b**) copper fin cooling and (**c**) aluminium fin cooling.

A similar behavior is observed for the copper fin which is shown in Figure 11b. However, for the aluminium fin (Figure 11c), it is observed that TC11 is slightly hotter than TC5. This is not always the case for the other samples, whereby TC5 can become hotter. This may be due to small variations in the positioning of the cell tabs within the busbar blocks which results in offsets between the exact positioning of the cell body under the fin surface, which may contribute to the shift of the hot spot between TC5 and TC11. For example, a slight offset in the positioning of the cell to the left would result in TC5 no longer overlaying the edge of the cell, thus positioning it further from the heat

generation source and, therefore, reducing the measurement value relative to TC11 which is still overlaying the cell material. This cause of variance is discussed further in Section 3.4, and may be more prominent for the cells cooled with lower thermally conductivity fins which incur greater temperature gradients across the fin body. For all analysed fin materials, the measured cold spot across the fin body is given by TC9, which is as expected due to its closest proximity to the cold plate.

Given that the temperature difference between TC5 and TC11 appears to be minimal, whereby the measured hot spot may, in some instances, interchange slightly between the two; the remainder of the analysis will focus on the measurements from TC5 and TC5–TC9, which are considered as $T_{max,f}$ and $\Delta T_{max,f}$ respectively. This is performed to provide consistent comparisons between the fin material samples and to enable an averaging of the values across the back fin samples given that these measurements are also present at these locations.

3.3. Comparisons between Fin Materials

For comparison between fin materials, the average values of TC5 and TC9 between the front and back fins are taken as the value for that given cell sample. The average value over all the individual cell samples is then taken to represent the value for the given material type and thermocouple location. A comparison of the average curve to those of each individual cell sample is shown for every electrical loading condition and fin type, which is contained in Appendix A for completeness.

3.3.1. C Thermal Response

The key temperature measurements for the fin surface during the 1 C discharge are displayed in Figure 12, where marker points are shown at increments of 500 s. From Figure 12a, it is observed that TC5 reaches a peak of 34.9 °C with the aluminium fin and a peak of 32.7 °C and 30.7 °C for the copper and k-core fins, respectively. From our previous work in Reference[12], it is suggested that the optimum temperature range of the 53 Ah cells may be in the region of 25–35 °C to maximise the battery performance whilst limiting the rate of high-temperature-related ageing mechanisms. Therefore, single-edge cooling of the cell with aluminium fins appears to be appropriate under this 1 C usage scenario, which may be a particularly aggressive yet realistic case for a large sized EV [44]. It is important to note, however, that the maximum temperature inside the cell will be larger than that recorded on the fin surface. An estimation of the temperature gradient throughout the cell could be achieved via a thermal modelling analysis which is an area for further work.
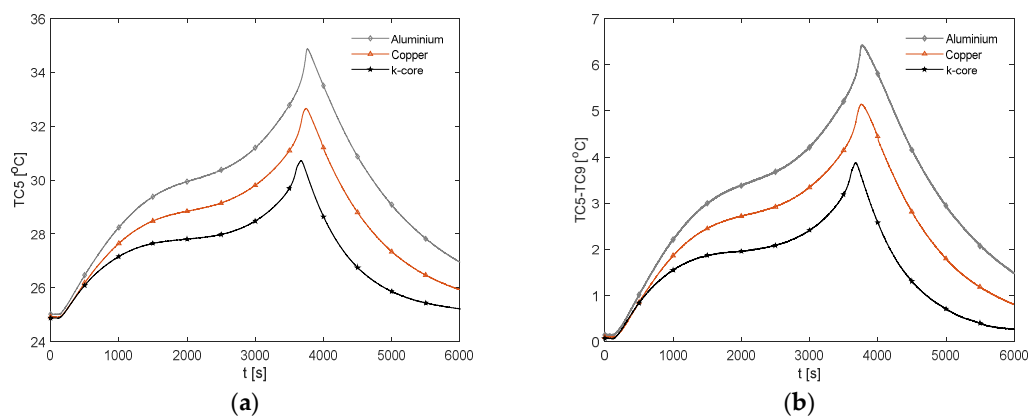

Figure 12. The 1 C discharge experimental results with (**a**) the TC5 measurements and (**b**) the TC5–TC9 measurements.

Figure 12b highlights that $\Delta T_{max,f}$ reaches 6.4 °C at the end of the 1 C discharge for the aluminium fin which is over the common recommended limit of 5 °C for the cell temperature gradient reported in the literature (as discussed in Section 1). Provided that the deep discharge region of the cell is avoided (e.g., limit the discharge to not enter below circa 10% SOC), it is possible to avoid the

majority of the large temperature increase of the cell during the final portions of the discharge to satisfy the 5 °C limit. However, the k-core fin is the only material that enables $\Delta T_{max,f}$ to remain below 5 °C for the whole discharge with a peak value of 3.9 °C. Evidently, the superior thermal conductivity of the k-core fin improves the heat removal rate to the exterior cold plate, allowing for both a reduced peak temperature and an improved temperature uniformity.

3.3.2. WLTP Class 3 Thermal Response

The temperature results for the WLTP Class 3 PHEV duty cycle are shown in Figure 13. Here, the k-core fin provides an average value for $T_{max,f}$ of 27.4 °C and $\Delta T_{max,f}$ of 1.7 °C across the duration of the duty cycle. For the aluminium and copper fins, the average values for $T_{max,f}$ are 29.1 °C and 28.4 °C respectively, with a corresponding average value for $\Delta T_{max,f}$ of 2.6 °C and 2.4°C. Relative to the 1 C discharge, the more dynamic nature of the drive cycle highlights a difference in the ability of the fin materials to thermally control the cell under more aggressive situations (i.e., periods of higher currents). Specifically, the higher in-plane thermal conductivity and high in-plane thermal diffusivity of the k-core material enable the thermal system to respond quicker to temperature fluctuations relative to the conventional materials. This can be seen during the less intensive portions of the duty cycle that follow an aggressive period (e.g., at t = 2000 s), where the fin and cell begin to cool at a much faster rate with the k-core material. This minimises the periods in which the cell is subject to the detrimental effects of elevated temperature. However, for this particular drive cycle, provided that the deep discharge region is avoided during commercial use to prevent the large spike in temperature, the use of the k-core fin (although preferable) may not be necessary, given that the aluminium fin offers a satisfactory thermal control. A more direct benefit of employing the k-core material for this electrical loading (also for the 1 C case) may be in enabling the use of thinner fins. This is since the extra thermal head room that is present with the current fin thickness may be traded for a thinner fin, which, when possible, is beneficial for reducing the mass and/or volume penalty of the BTMS.
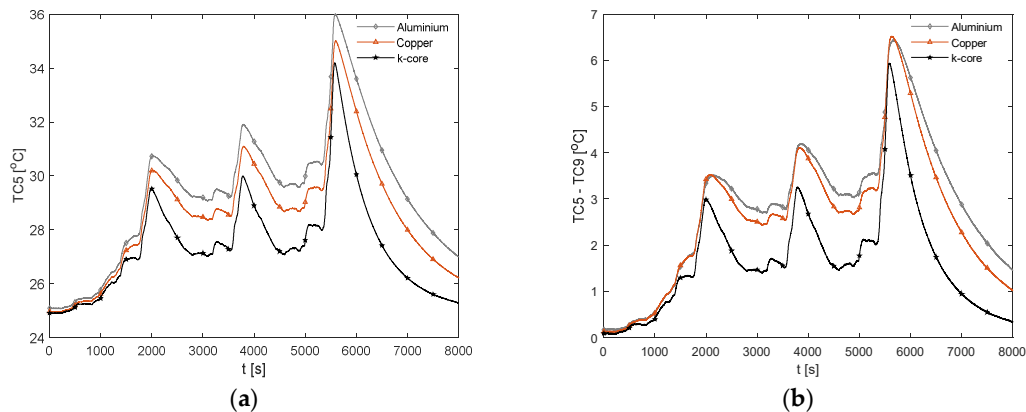

Figure 13. The WLTP Class 3 experimental results with (**a**) the TC5 measurements and (**b**) the TC5–TC9 measurements.

3.3.3. C and 3 C Discharge Thermal Response

For the more aggressive 2 C and 3 C electrical loading conditions, the improvement of the k-core fin over conventional aluminium in reducing $T_{max,f}$ becomes more apparent. From Figure 14a for the 2 C discharge, the k-core fin provides a reduction in the peak value of $T_{max,f}$ of 15.1% relative to aluminium. Figure 15a for the 3 C case provides a similar reduction of 14.7%, whereby $T_{max,f}$ for the k-core fin is 45.6 °C at the end of the discharge and is the only fin material capable of remaining below 50 °C. As recommended by Sato [49], this threshold should not be surpassed for a lithium-ion battery to avoid an accelerated degradation and reduced cycle life. Thomas et al. [50] also reported significant increases in the power fade of lithium-ion batteries when exposed to temperatures above 45 °C, where

they experimentally observed the power fade increasing from circa 22% at 45 °C to circa 33% at 55 °C after 20 weeks of soak time at the given temperature when stored at 60% SOC.
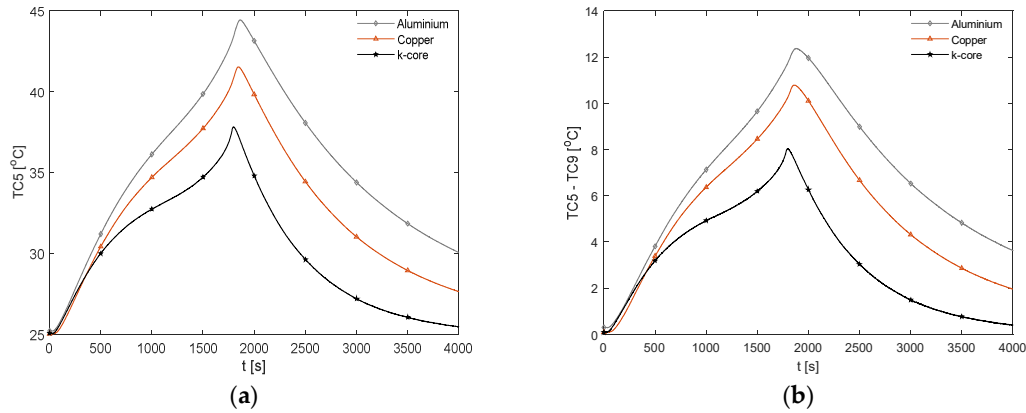

Figure 14. The 2 C discharge results with (**a**) the TC5 measurements and (**b**) the TC5–TC9 measurements.

Figures 14a and 15b demonstrate the evolution of $\Delta T_{max,f}$ for each fin material during the 2C and 3C discharge respectively. Relative to aluminium, the k-core fin results in a decrease in the peak value of $\Delta T_{max,f}$ of 35.5% and 26.8% during the 2C and 3C discharge respectively. The greater reduction for the 2C discharge may be due to the greater duration of the cycle and lower battery heat generation rate, which allows for the thermal profile of the cell and fin to more fully develop prior to the cell reaching the cutoff voltage. However, neither fin material is able to limit $\Delta T_{max,f}$ to below 5 °C during either discharge.
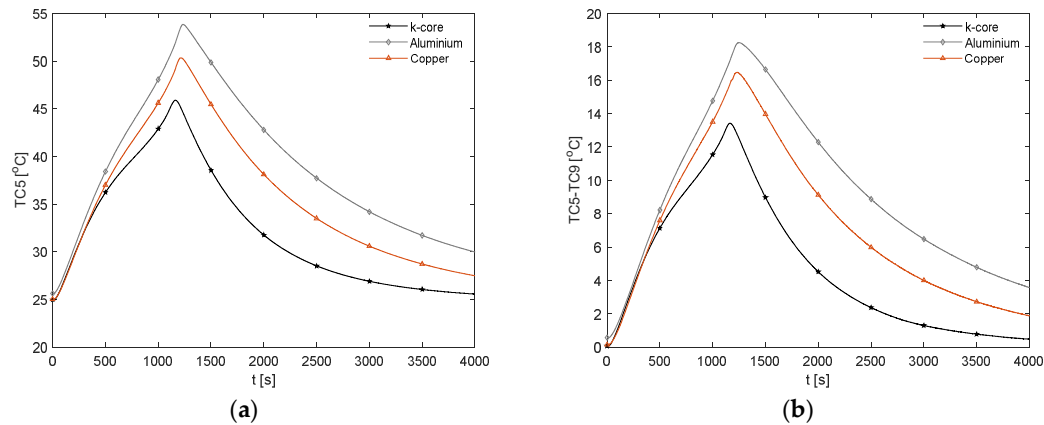
Figure 15. The 3 C discharge results with (**a**) the TC5 measurements and (**b**) the TC5–TC9 measurements.

3.3.4. Race Cycle Thermal Response

The temperature results during the race duty cycle are shown in Figure 16. Whilst the k-core fin provides an appreciable reduction in $T_{max,f}$ and $\Delta T_{max,f}$ relative to both aluminium and copper, the k-core fin still results in large values for $T_{max,f}$ of 44.9 °C and $\Delta T_{max,f}$ of 13.0 °C. As with the 2 C and 3 C discharges, this points towards a limitation in the ability of this particular fin-based BTMS during more aggressive conditions. This may be due to cooling only one edge of the fin, particularly for this analysed pouch cell where the heat transfer pathway between the non-cooled edge of the fin and the cooled edge is long, resulting in a larger thermal resistance. Single-edge cooling, even with the k-core fin, may, therefore, be an inadequate thermal management choice when subject to long-term track racing use due to both the excessive peak temperature and surface temperature gradient.

It is also important to analyse the cooldown period (i.e., the period following the completion of the duty cycle where the cell current is zero) between the different fin materials. Here, it is observed that the k-core fin cools rapidly relative to the other materials. For instance, it takes the aluminium fin 18.9 minutes to cool from 44 °C to 34 °C, 14.3 minutes for the copper fin and 9.5 minutes for the k-core fin. This may enable potential efficiency savings for the control system when employing a k-core fin-based BTMS, given that the active thermal control system could be disengaged sooner than when employing the less thermally conductive materials which require a longer cooldown period.
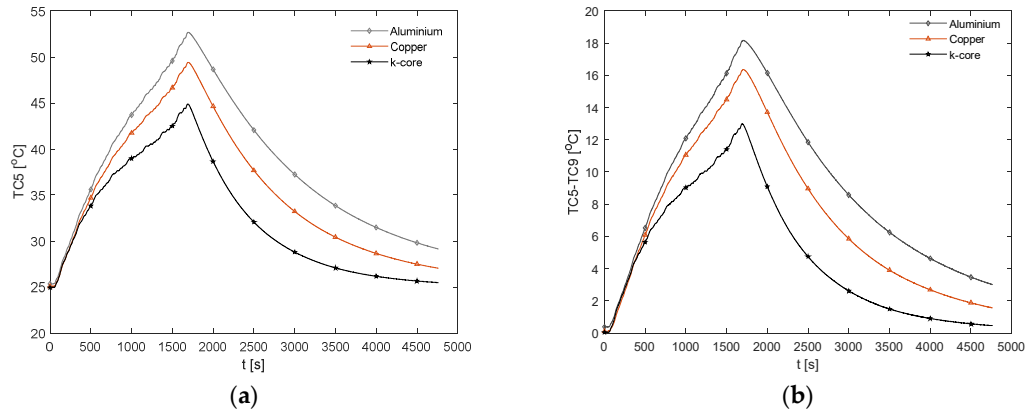
Figure 16. The race cycle results with (**a**) the TC5 measurements and (**b**) the TC5–TC9 measurements.

3.3.5. Comparisons Summary

A summary of the key thermal parameters taken at the end of each analysed electrical loading scenario is shown in Table 3.

Table 3. A summary of the averaged values of the recorded maximum fin temperature and fin temperature gradient at the end of each test case.

Fin Material	Test Case									
	Race		3C		2C		WLTP Class 3		1C	
	TC5 (°C)	$\Delta T_{max,f}$ (°C)	TC5 (°C)	$\Delta T_{max,f}$ (°C)	TC5 (°C)	$\Delta T_{max,f}$ (°C)	TC5 (°C)	$\Delta T_{max,f}$ (°C)	TC5 (°C)	$\Delta T_{max,f}$ (°C)
Aluminium	52.7	18.2	53.8	18.3	44.5	12.4	36.0	6.5	34.9	6.4
Copper	49.4	16.4	50.3	16.5	41.5	10.8	35.0	6.5	32.7	5.1
k-core	44.9	13.0	45.9	13.4	37.8	8.0	34.2	5.9	30.7	3.9
	Race		3C		2C		WLTP Class 3		1C	
	TC5 (°C)	$\Delta T_{max,f}$ (°C)	TC5 (°C)	$\Delta T_{max,f}$ (°C)	TC5 (°C)	$\Delta T_{max,f}$ (°C)	TC5 (°C)	$\Delta T_{max,f}$ (°C)	TC5 (°C)	$\Delta T_{max,f}$ (°C)
k-core fin % decrease relative to aluminium (%)	14.8	28.6	14.7	26.8	15.1	35.5	5.0	9.2	12.0	39.1
k-core fin % decrease relative to copper (%)	9.1	20.7	8.7	21.8	8.9	25.9	2.3	9.2	6.1	23.5

3.4. Error Analysis

A statistical analysis highlighting the results of the standard deviation and standard error of the TC5 and TC9 measurements is shown in Table 4. The results for the aluminium WLTP Class 3 and k-core fin 2 C condition are not applicable given that only a single sample is achieved for each of these conditions.

Sources of experimental variation between the samples may be due to slight offsets in the cell position within the busbar blocks, which alters the alignment of the thermocouple locations relative

to the cell location. An example of an offset in the position of the cell to the left is represented schematically in Figure 17.

Table 4. The statistical data from the obtained samples at the end of each test case.

		Mean			Standard Deviation			Standard Error		
Test Case	**Fin Material**	TC5 (°C)	TC9 (°C)	$\Delta T_{max,f}$ (°C)	TC5 (°C)	TC9 (°C)	$\Delta T_{max,f}$ (°C)	TC5 (°C)	TC9 (°C)	$\Delta T_{max,f}$ (°C)
1 C	Aluminium	34.52	28.56	5.96	0.50	0.15	0.65	0.36	0.11	0.46
	Copper	32.74	27.57	5.16	0.23	0.25	0.41	0.12	0.13	0.20
	k-core	30.88	26.95	3.92	0.22	0.06	0.23	0.11	0.03	0.12
WLTP Class 3	Aluminium	-	-	-	-	-	-	-	-	-
	Copper	35.01	28.48	6.53	0.53	0.34	0.19	0.38	0.24	0.14
	k-core	34.19	28.24	5.94	0.22	0.33	0.11	0.16	0.23	0.08
2 C	Aluminium	44.54	32.13	12.41	0.69	0.61	1.03	0.31	0.27	0.46
	Copper	41.57	30.77	10.81	0.43	0.45	0.67	0.18	0.19	0.27
	k-core	-	-	-	-	-	-	-	-	-
3 C	Aluminium	53.88	35.59	18.30	1.12	0.89	1.60	0.50	0.40	0.72
	Copper	50.43	34.04	16.39	0.38	0.53	0.78	0.16	0.22	0.32
	k-core	46.19	32.63	13.56	0.48	0.18	0.39	0.20	0.07	0.16
Race cycle	Aluminium	52.69	34.52	18.18	0.92	0.78	1.41	0.46	0.39	0.70
	Copper	49.43	33.05.	16.37	0.70	0.69	0.77	0.31	0.31	0.34
	k-core	44.90	31.89	13.02	0.47	0.29	0.37	0.21	0.13	0.16
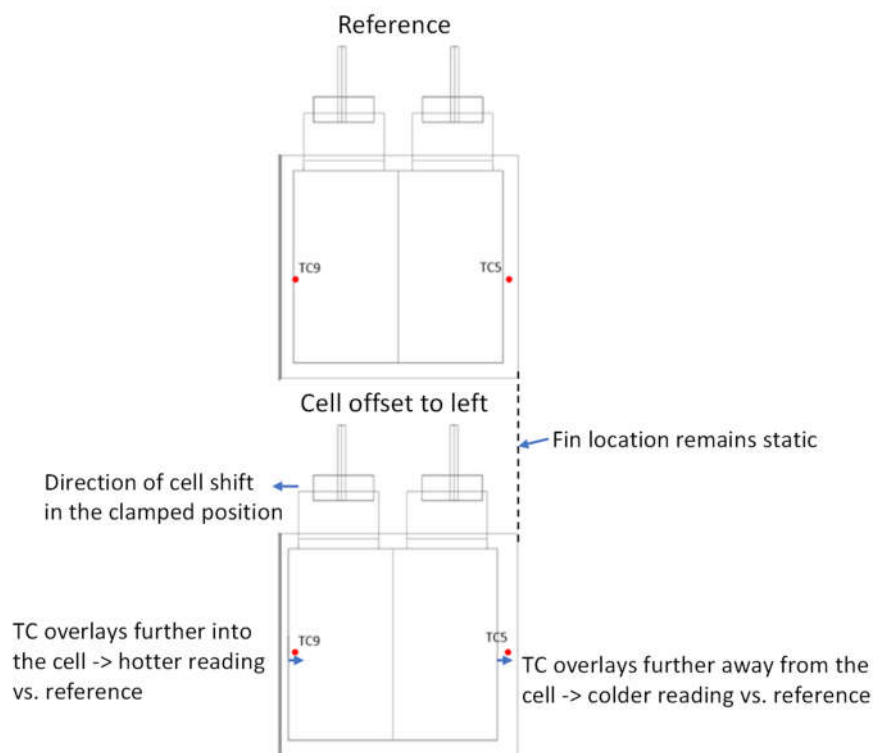
Figure 17. The potential causes of variation due to the fin body and cell being offset between samples.

As shown, the offset results in the location of TC5 now being further from the cell body, which may result in a lower reading than the reference position where TC5 is positioned closer to the heat generation source. Similarly, as TC5 is now positioned to the left, TC9 is in turned positioned to overlay further across the cell and, therefore, is further from the cold plate. This effect may increase

the reading of TC9 relative to the reference case without any offset. An example of an offset in the cell tab positioning to the left may have occurred for Cell 3 during the copper fin experiments, as this would explain why it consistently has one of the highest TC9 readings yet also the lowest TC5 reading when compared to the other samples (see Figures A6–A10 in Appendix A).

3.5. Mass and Volume Considerations

As the analysed fin material samples do not have the exact dimension and thickness (although similar), it is important to investigate their impact on both a mass and volume basis.

A volume packing metric ($V_{m,p}$) can be defined, which considers the thickness of the fin in relation to the cell thickness.

$$V_{m,p} = \frac{Cell\ thickness}{Cell\ thickness + fin\ thickness} \tag{4}$$

where $V_{m,p}$ is the volume packing metric. Values closer to unity for $V_{m,p}$ are conducive towards a more compact thermal management design. Table 5 summarises the results of the analysis, which also includes the % increase in weight of the cell with the cooling fins. The mass of the cells is 1.15 kg.

Table 5. The mass increase and packing metric as a function of fin material.

Method	Increased Weight Added to Cell (%)	$V_{m,p}$
Aluminium	12.9	0.92
Copper	44.9	0.92
k-core	12.9	0.90

Table 5 highlights that 1-edge cooling with k-core and aluminium adds circa 13% weight to the cell. Methods to reduce the mass impact of the fin cooling method could be achieved by optimising the geometry of the fin, given that these analysed prototype samples are slightly oversized for the cell body. The weight increase for the copper fin adds more than 40% extra weight for the cell, rendering it unsuitable as a cooling material.

The presence of the skin layer with the k-core fin decreases the volume packing compactness from 0.92 with the conventional fins to 0.90 with the k-core fin. The total fin thickness could be reduced through decreasing the APG thickness or altering the skin layer properties. The effect of this on the fin thermal performance is a scope for further work.

The effectiveness of the fin materials in their ability to minimise the formed temperature gradients on a mass basis can also be expressed by the specific delta temperature, which considers the reciprocal of the product of the peak value of $\Delta T_{max,f}$ and the total fin mass per cell in this instance. Larger values for the specific delta temperature point towards a greater thermal efficiency on a mass basis. The results for the specific delta temperature as a function of fin material for each test case are shown in Figure 18. Here, the k-core fin provides an increase in the specific delta temperature between 10–64% relative to aluminium across all the tested scenarios. The lowest increase is for the WLTP Class 3 cycle, which may be due to the rapid increase in temperature as the cell reaches the cutoff voltage which cannot be compensated for by the BTMS. Also observed is that the specific delta temperature decreases for all materials as the aggressiveness of the test case increases. Methods to improve the mass efficiency of the system, such as the potential for two-edge cooling to reduce the thermal path between the cell and external cooling source, should be investigated for these use cases (particularly for the 3 C discharge and the race cycle).
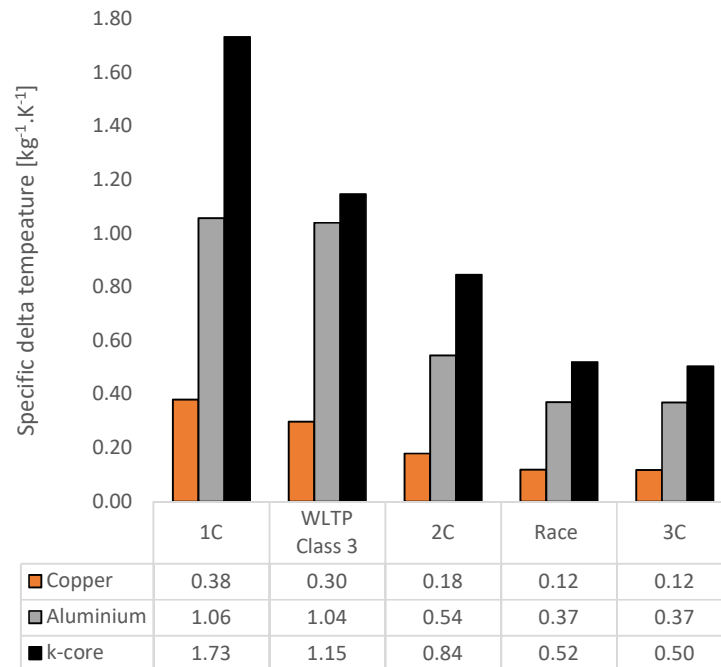
Figure 18. The specific delta temperature.

	1C	WLTP Class 3	2C	Race	3C
Copper	0.38	0.30	0.18	0.12	0.12
Aluminium	1.06	1.04	0.54	0.37	0.37
k-core	1.73	1.15	0.84	0.52	0.50

4. Further Work

Given the thermal improvement of the k-core over the reference case fins, further work should seek to analyse the effect of the improved gradient and peak temperature on the ageing rate of the cells. This would require a long-term testing of cells cooled with k-core fins and separate cells with aluminium fins under exact external cooling and electrical loading conditions.

As the presented test rig with k-core fin cooling requires the edge of the fin to be bent with a large 25 mm of contact length, a more practical edge cooling approach should be investigated to enable the compact packing of cells. The suitability of other encapsulating materials, such as Kapton, and the effect of the APG core thickness on thermal performance should also be investigated to further lower the mass and volume penalty associated with the k-core fins. In addition, as the material is currently produced on a level to supply niche sectors (such as aerospace), a cost analysis should be performed to investigate the potential of increased economies of scale to allow the penetration of the material into the commercial EV, PHEV and HEV markets.

The development of a thermal model to estimate the temperature profile throughout the cell under both single- and two-edge fin cooling is also an area for further work. Performing additional experiments to determine the difference in contact resistance between the more flexible k-core fin and conventional aluminium fins may further guide the choice of whether a thermal interface material is required in practical applications.

5. Conclusions

A comprehensive thermal analysis has been performed on a conduction-based method for cooling the surface of large format pouch cells, where a novel fin material with superior in-plane thermal conductivity is presented.

Of the considered cell electrical loading conditions, the experimental results reveal that 1-edge fin cooling pouch cells with k-core sheets (comprised of an annealed pyrolytic graphite core encapsulated in an aluminium foil) can provide a reduction in both the maximum fin temperature and temperature gradient of up to 15% and 39%, respectively, relative to conventional aluminium fins. The advantage of k-core is more prominent for the more aggressive electrical loading conditions, such as the performance electric vehicle (EV) duty cycle where the maximum recorded temperature

can remain below 45 °C, whilst the aluminium fins reach a temperature of 53 °C. This enables the cells cooled with k-core fins to operate within a far safer tolerance, given the accelerated ageing rates associated with operating at temperatures exceeding circa 50 °C reported in the literature. However, whilst the k-core fin also provides a greater temperature uniformity across the fin surface (13.0 °C measured gradient vs. 18.2 °C for aluminium), the value is still much larger than the recommended 5 °C limit reported in the literature. Further work should seek to investigate methods to improve the heat transfer rate for these aggressive applications, such as by cooling both edges of the fin or investigating the effect of increasing the fin thickness.

For the less aggressive tested electrical loading conditions (1 C and the plug-in hybrid vehicle (PHEV) cycle), the aluminium fin may provide a satisfactory thermal control given that the maximum temperature and temperature gradient remain below 35 °C and 5 °C for the majority of the test period. The benefit of k-core fins for these applications may be in the use of thinner fins to further reduce the mass and volume requirements of the battery thermal management system (BTMS), given the larger thermal head room available and their superior efficiency on a mass basis to reduce the temperature gradient (63% more efficient that the aluminium fin for the 1 C discharge). The determination of the optimum fin thickness for these applications is a scope for further work. The tested copper fins are unsuitable as a fin material for a BTMS given the large weight incurred to the cell, where the mass increase is 44.9% versus 12.9% for both the aluminium and k-core fins.

The promising results of this work act to advance the understanding on the thermal performance of conduction-based cooling for large format lithium-ion batteries, which may, in turn, accelerate the adoption of future lightweight, inherently safer fin cooling designs for automotive battery systems.

Conflicts of Interest: The authors declare no conflict of interest.

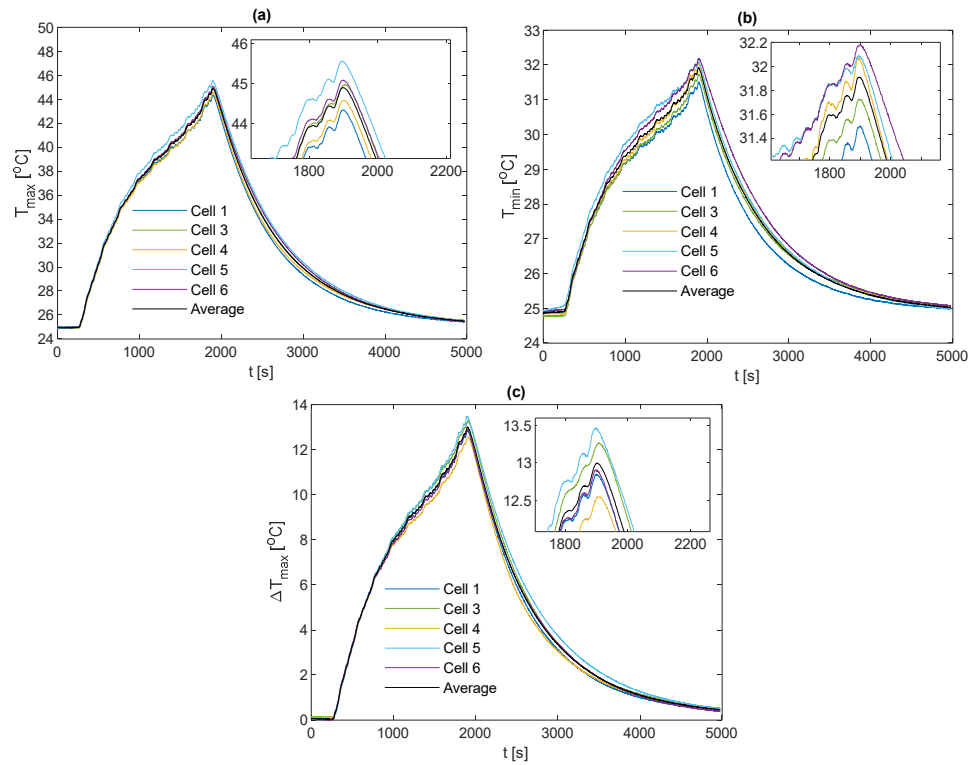## Appendix A. Individual Sample Temperature Measurements

Figure A1. The k-core fin race duty cycle results for all the tested cell samples with (**a**) the TC5 measurements, (**b**) the TC9 measurements and (**c**) the maximum fin temperature gradient (TC5–TC9).
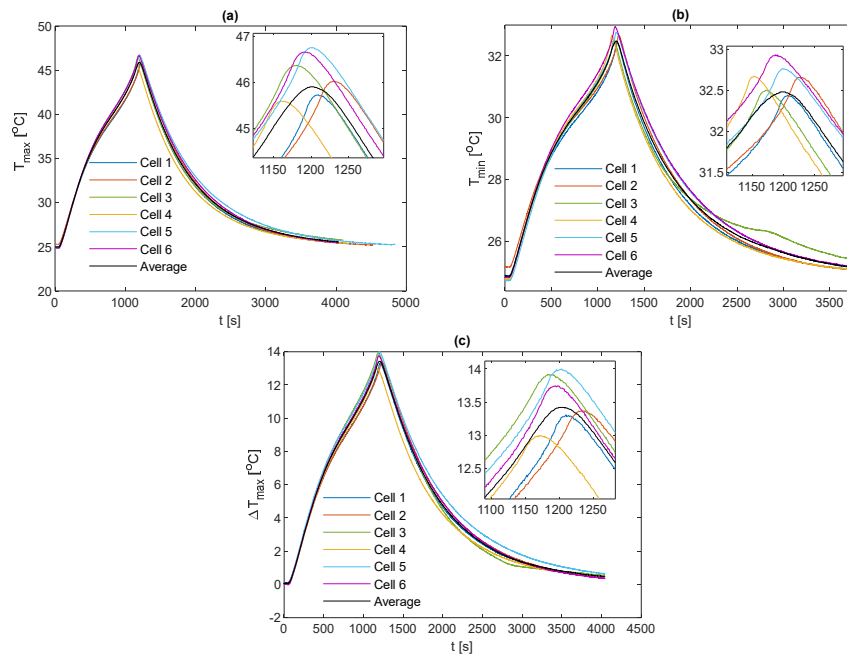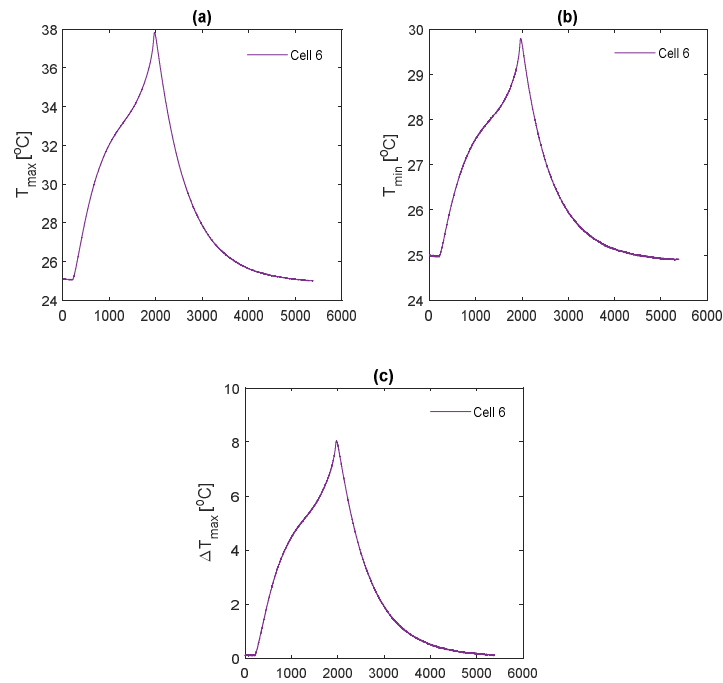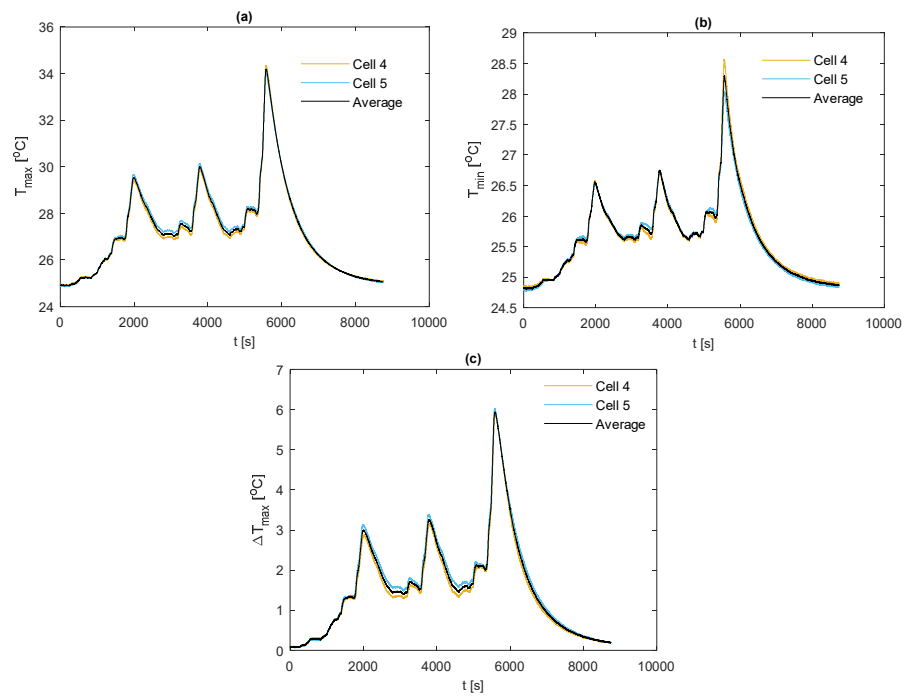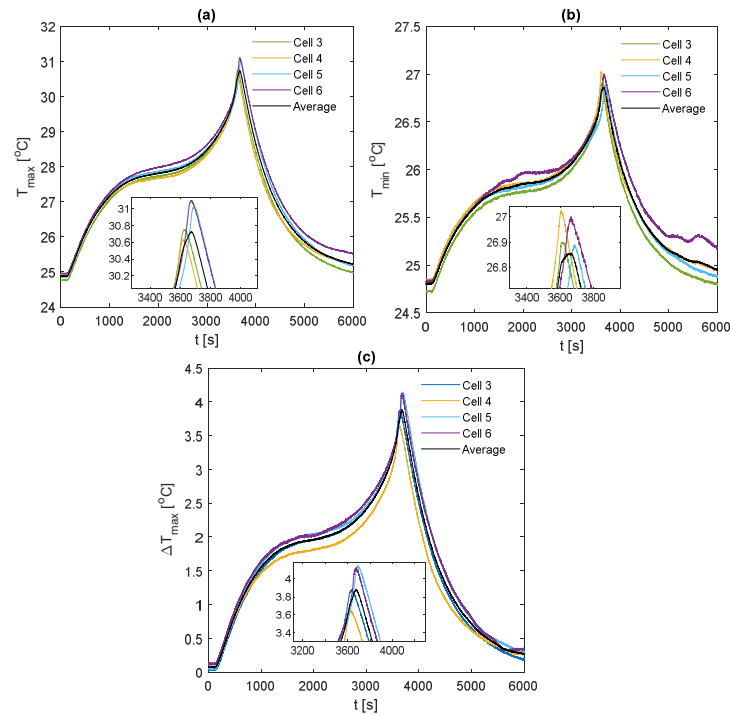

Figure A2. The k-core fin 3 C results for all the tested cell samples with (**a**) the TC5 measurements, (**b**) the TC9 measurements and (**c**) the maximum fin temperature gradient (TC5–TC9).
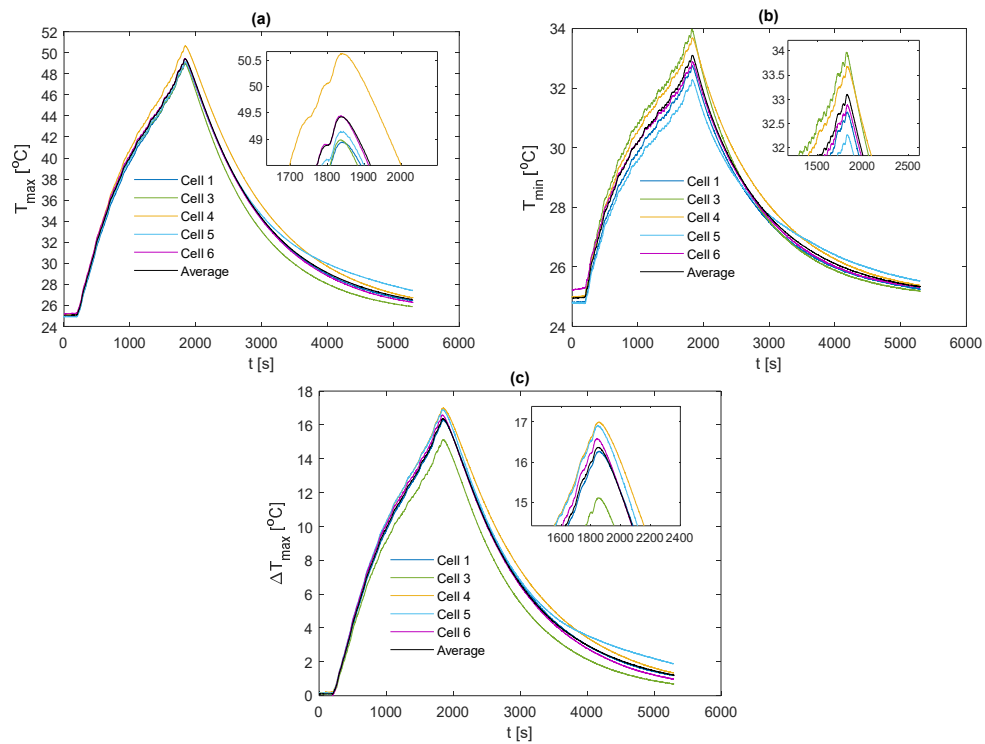
Figure A3. The k-core fin 2 C results for all the tested cell samples with (**a**) the TC5 measurements, (**b**) the TC9 measurements and (**c**) the maximum fin temperature gradient (TC5–TC9).
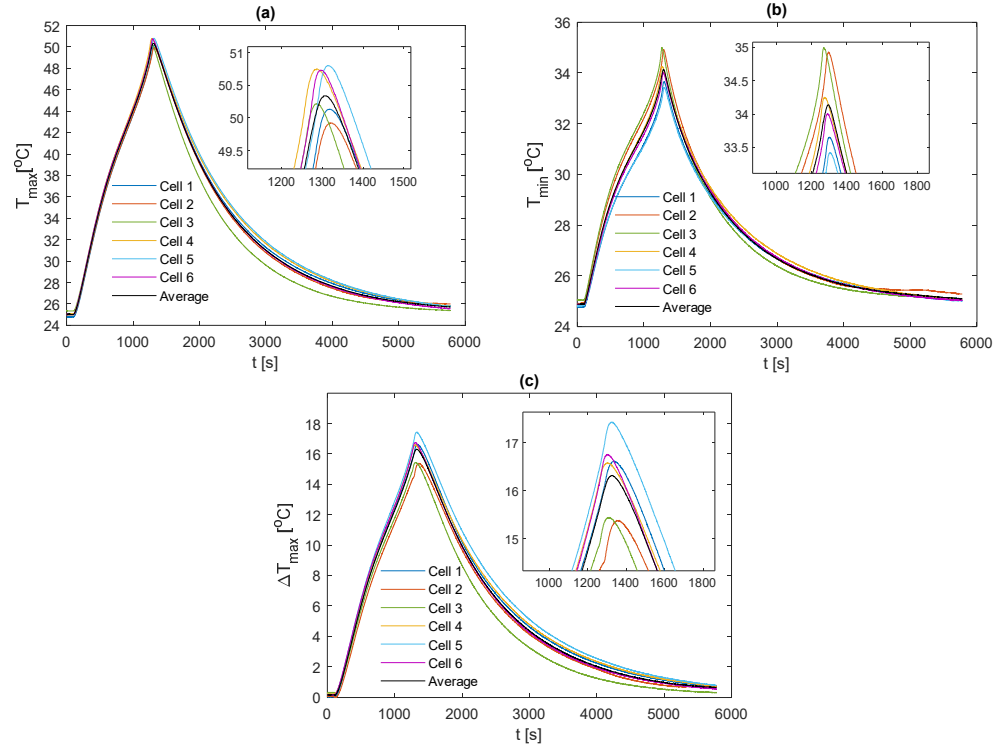

Figure A4. The k-core fin WLTP Class 3 duty cycle results for all the tested cell samples with (**a**) the TC5 measurements, (**b**) the TC9 measurements and (**c**) the maximum fin temperature gradient (TC5–TC9).

Figure A5. The k-core fin 1C discharge results for all the tested cell samples with (**a**) the TC5 measurements, (**b**) the TC9 measurements and (**c**) the maximum fin temperature gradient (TC5–TC9).
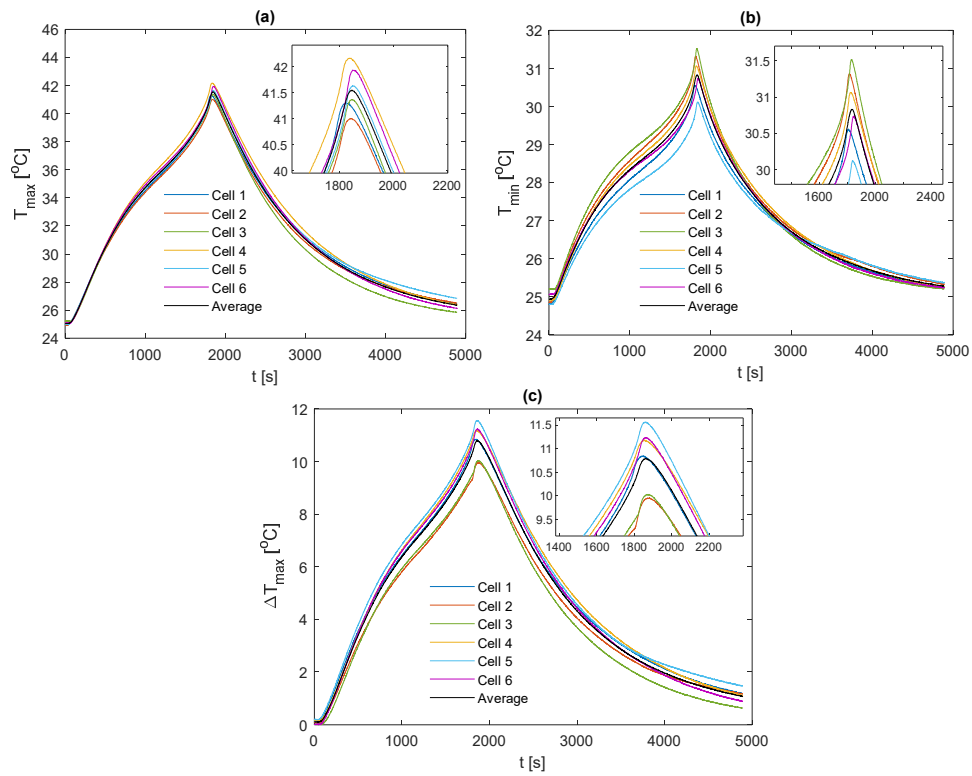

Figure A6. The copper fin race duty cycle results for all the tested cell samples with (**a**) the TC5 measurements, (**b**) the TC9 measurements and (**c**) the maximum fin temperature gradient (TC5–TC9).

Figure A7. The copper fin 3 C discharge results for all the tested cell samples with (**a**) the TC5 measurements, (**b**) the TC9 measurements and (**c**) the maximum fin temperature gradient (TC5–TC9).
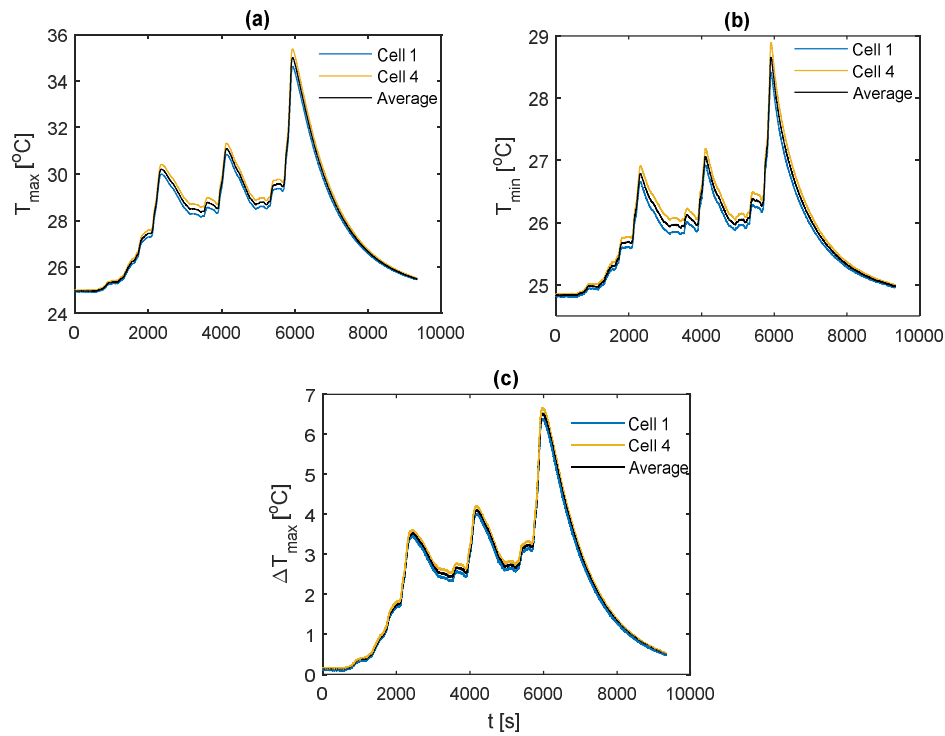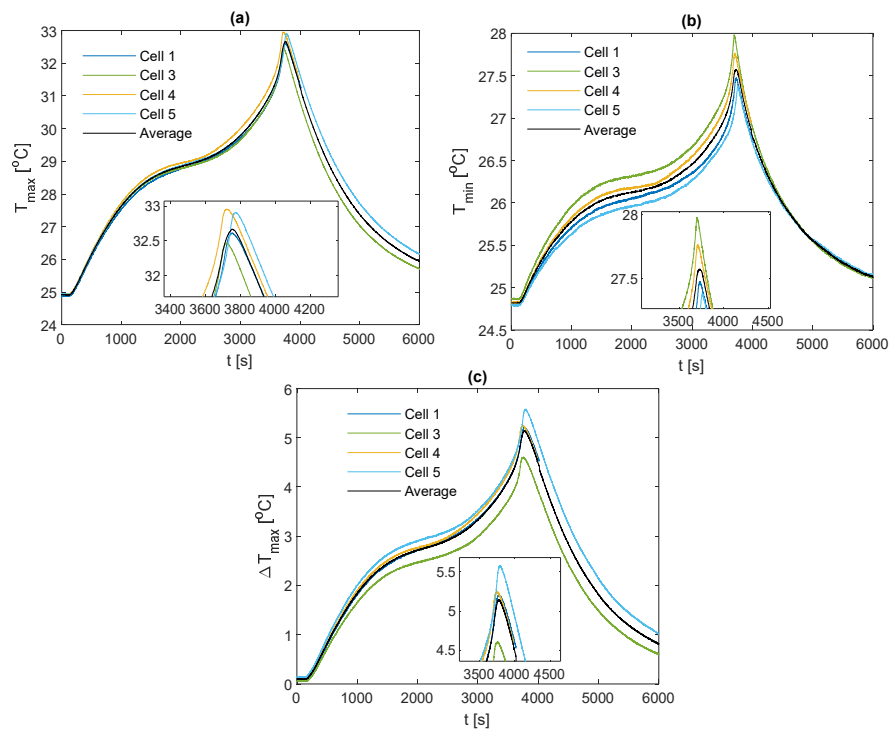

Figure A8. The copper fin 2 C discharge results for all the tested cell samples with (**a**) the TC5 measurements, (**b**) the TC9 measurements and (**c**) the maximum fin temperature gradient (TC5–TC9).

Figure A9. The copper fin WLTP Class 3 duty cycle results for all the tested cell samples with (**a**) the TC5 measurements, (**b**) the TC9 measurements and (**c**) the maximum fin temperature gradient (TC5–TC9).

Figure A10. The copper fin 1 C discharge results for all the tested cell samples with (**a**) the TC5 measurements, (**b**) the TC9 measurements and (**c**) the maximum fin temperature gradient (TC5–TC9).
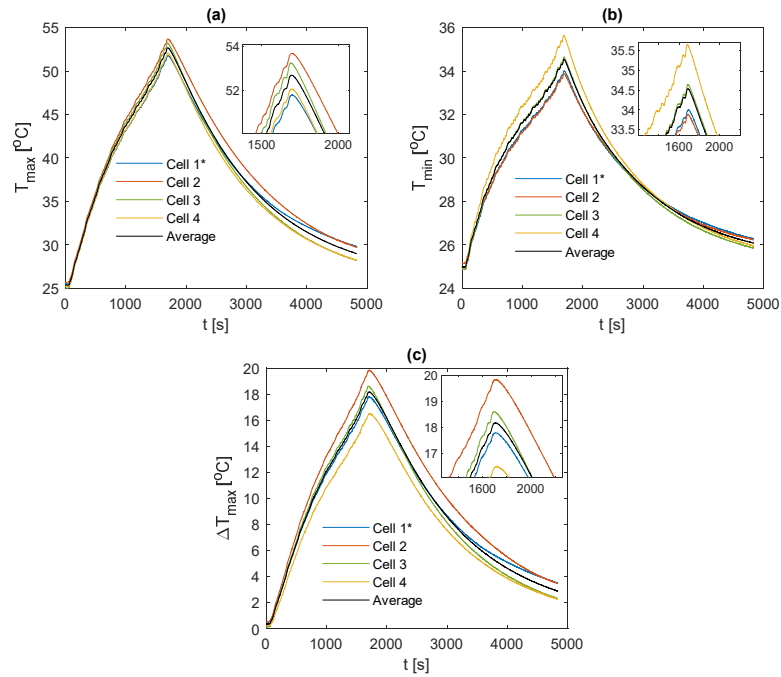
Figure A11. The aluminium fin race duty cycle results for all the tested cell samples with (**a**) the TC5 measurements, (**b**) the TC9 measurements and (**c**) the maximum fin temperature gradient (TC5–TC9).
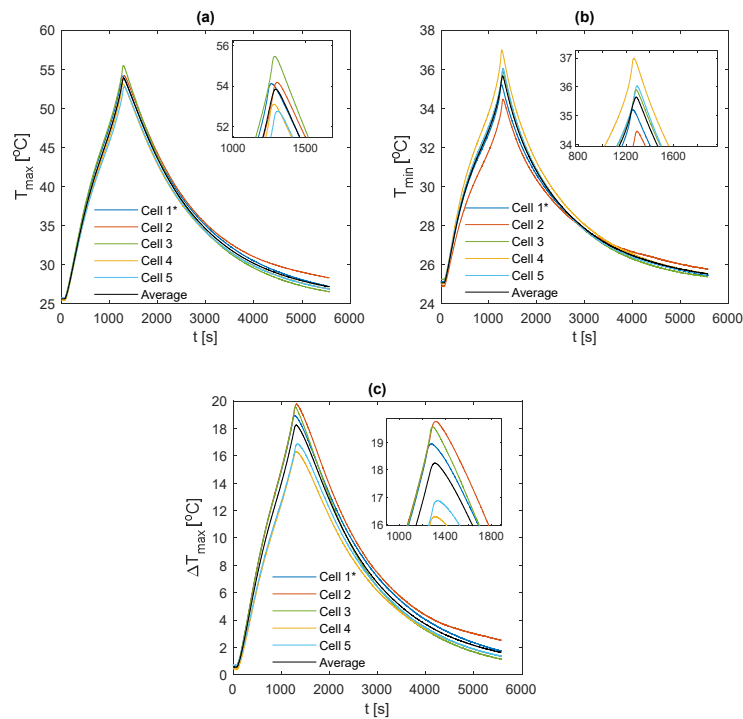

Figure A12. The aluminium fin 3 C discharge results for all the tested cell samples with (**a**) the TC5 measurements, (**b**) the TC9 measurements and (**c**) the maximum fin temperature gradient (TC5–TC9).
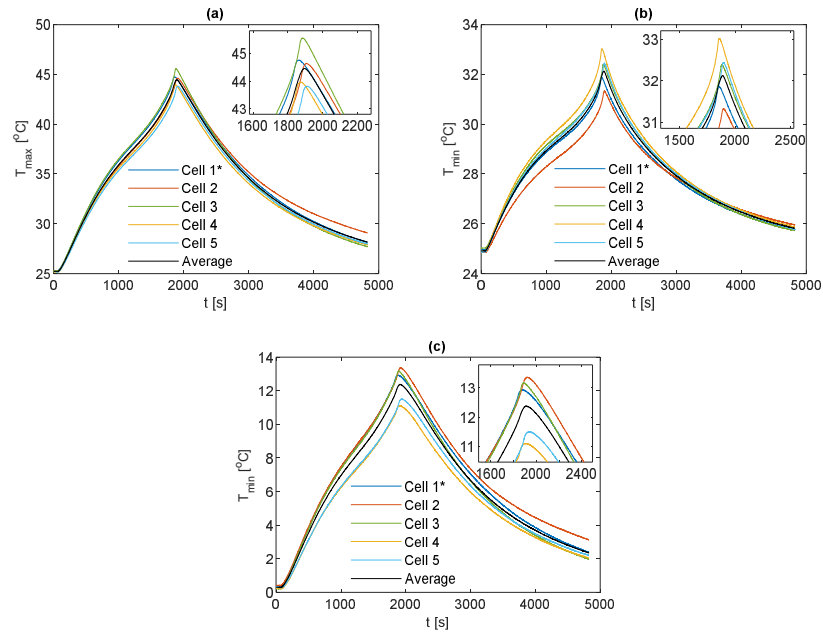
Figure A13. The aluminium fin 2 C discharge results for all the tested cell samples with (**a**) the TC5 measurements, (**b**) the TC9 measurements, (**c**) the maximum fin temperature gradient (TC5–TC9).
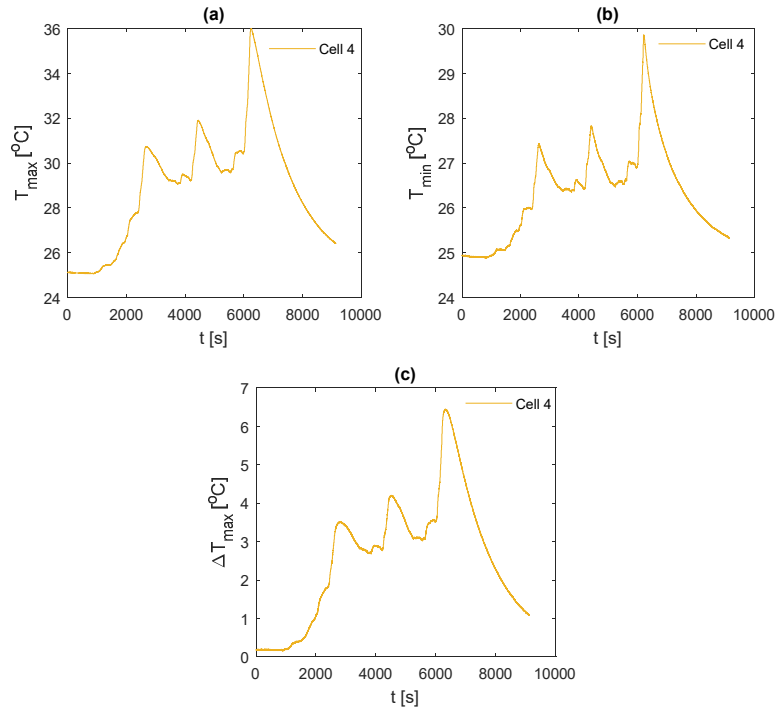

Figure A14. The aluminium fin WLTP Class 3 cycle results for all the tested cell samples with (**a**) the TC5 measurements, (**b**) the TC9 measurements and (**c**) the maximum fin temperature gradient (TC5–TC9).
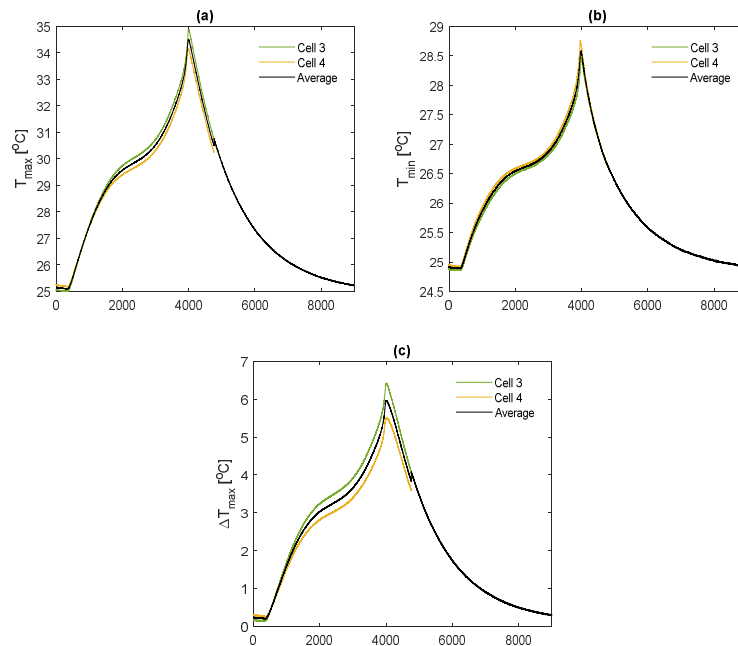
Figure A15. The aluminium fin 1 C discharge results for all the tested cell samples with (**a**) the TC5 measurements, (**b**) the TC9 measurements and (**c**) the maximum fin temperature gradient (TC5–TC9).

References

1. Ford Media Center. Ford Adding Electrified F-150, Mustang, Transit by 2020 in Major EV push; Expanded U.S. Plant to Add 700 Jobs to Make EVS, Autonomous Cars. 2017. Available online: https://media.ford.com/content/fordmedia/fna/us/en/news/2017/01/03/ford-adding-electrified-f-150-mustang-transit-by-2020.html (accessed on 29 March 2018).
2. Tesla Motors. *Tesla Fourth Quarter & Full Year 2017 Update*; Tesla: Palo Alto, CA, USA, 2017.
3. Volkswagen. *New Group Strategy Adopted: Volkswagen Group to Become a World-Leading Provider of Sustainable Mobility*; Volkswagen: Berlin, Germany, 2016.
4. International Energy Agency. *Global EV Outlook 2017: Two Million and Counting*; International Energy Agency: Paris, France, 2017.
5. Goldman Sachs Global Investment Research. *Electric Vehicle Boom: ICE-ing The Combustion Engine*; Goldman Sachs: New York, NY, USA, 2017.
6. Yoo, H.D.; Markevich, E.; Salitra, G.; Sharon, D.; Aurbach, D. On the challenge of developing advanced technologies for electrochemical energy storage and conversion. *Mater. Today* **2014**, *17*, 110–121.
7. Blomgren, G.E. The Development and Future of Lithium Ion Batteries. *J. Electrochem. Soc.* **2017**, *164*, 5019–5025.
8. Bandhauer, T.M.; Garimella, S.; Fuller, T.F. A Critical Review of Thermal Issues in Lithium-Ion Batteries. *J. Electrochem. Soc.* **2011**, *158*, R1.
9. Waldmann, T.; Wilka, M.; Kasper, M.; Fleischhammer, M.; Wohlfahrt-Mehrens, M. Temperature dependent ageing mechanisms in Lithium-ion batteries—A Post-Mortem study. *J. Power Sources* **2014**, *262*, 129–135.
10. Pesaran, G.K.A.; Santhanagopalan, S. Addressing the Impact of Temperature Extremes on Large Format Li-Ion Batteries for Vehicle Applications. In Proceedings of the 30th International Battery Seminar, Ft. Lauderdale, FL, USA, 11–14 March 2013.
11. Tourani, A.; White, P.; Ivey, P. Analysis of electric and thermal behaviour of lithium-ion cells in realistic driving cycles. *J. Power Sources* **2014**, *268*, 301–314.

12. Hosseinzadeh, E.; Genieser, R.; Worwood, D.; Barai, A.; Marco, J.; Jennings, P. A systematic approach for electrochemical-thermal modelling of a large format lithium-ion battery for electric vehicle application. *J. Power Sources* **2018**, *382*, 77–94.

13. Wang, Q.; Ping, P.; Zhao, X.; Chu, G.; Sun, J.; Chen, C. Thermal runaway caused fire and explosion of lithium ion battery. *J. Power Sources* **2012**, *208*, 210–224.

14. Wang, Q.; Jiang, B.; Li, B.; Yan, Y. A critical review of thermal management models and solutions of lithium-ion batteries for the development of pure electric vehicles. *Renew. Sustain. Energy Rev.* **2016**, *64*, 106–128.

15. Hunt, I.A.; Zhao, Y.; Patel, Y.; Offer, J. Surface Cooling Causes Accelerated Degradation Compared to Tab Cooling for Lithium-Ion Pouch Cells. *J. Electrochem. Soc.* **2016**, *163*, 1846–1852.

16. Greco, A.; Cao, D.; Jiang, X.; Yang, H. A theoretical and computational study of lithium-ion battery thermal management for electric vehicles using heat pipes. *J. Power Sources* **2014**, *257*, 344–355.

17. Ye, Y.; Saw, L.H.; Shi, Y.; Tay, A.A.O. Numerical analyses on optimizing a heat pipe thermal management system for lithium-ion batteries during fast charging. *Appl. Therm. Eng.* **2015**, *86*, 281–291.

18. Pesaran, A. Battery thermal models for hybrid vehicle simulations. *J. Power Sources* **2002**, *110*, 377–382.

19. Tran, T.-H.; Harmand, S.; Sahut, B. Experimental investigation on heat pipe cooling for Hybrid Electric Vehicle and Electric Vehicle lithium-ion battery. *J. Power Sources* **2014**, *265*, 262–272.

20. Zhao, R.; Gu, J.; Liu, J. An experimental study of heat pipe thermal management system with wet cooling method for lithium ion batteries. *J. Power Sources* **2015**, *273*, 1089–1097.

21. Pesaran, A. Battery Thermal Management in EVs and HEVs : Issues and Solutions. *Adv. Automot. Batter. Conf.* **2001**, *43*, 34–49.

22. Grandjean, T.; Barai, A.; Hosseinzadeh, E.; Guo, Y.; Mcgordon, A.; Marco, J. Large format lithium ion pouch cell full thermal characterisation for improved electric vehicle thermal management. *J. Power Sources* **2017**, *359*, 215–225.

23. Fan, L.; Khodadadi, J.M.; Pesaran, A.A. A parametric study on thermal management of an air-cooled lithium-ion battery module for plug-in hybrid electric vehicles. *J. Power Sources* **2013**, *238*, 312–2013.

24. Rao, Z.; Wang, S. A review of power battery thermal energy management. *Renew. Sustain. Energy Rev.* **2011**, *15*, 4554–4571.

25. Kim, G.H.; Pesaran, A. Battery Thermal Management System Design Modeling. In Proceedings of the 22nd International Batter, Hybrid Fuel Cell Electric Vehicle Symposium & Exposition (EVS22), Yokohama, Japan, 23–28 October 2006; Volume 1, pp. 126–133.

26. Giuliano, M.R.; Advani, S.G.; Prasad, A.K. Thermal analysis and management of lithium-titanate batteries. *J. Power Sources* **2011**, *196*, 6517–6524.

27. Mohammadian, S.K.; Zhang, Y. Thermal management optimization of an air-cooled Li-ion battery module using pin- fi n heat sinks for hybrid electric vehicles. *J. Power Sources* **2015**, *273*, 431–439.

28. Park, S.; Jung, D. Battery cell arrangement and heat transfer fluid effects on the parasitic power consumption and the cell temperature distribution in a hybrid electric vehicle. *J. Power Sources* **2013**, *227*, 191–198.

29. Tesla Motors. Battery Coolant Jacket. U.S. Patent 8647763B2, 30 June 2011.

30. Chevrolet. *2016 Chevrolet Volt Battery System*; Chevrolet: Detroit, MI, USA, 2016.

31. Huo, Y.; Rao, Z.; Liu, X.; Zhao, J. Investigation of power battery thermal management by using mini-channel cold plate. *Energy Convers. Manag.* **2015**, *89*, 387–395.

32. Panchal, S.; Khasow, R.; Dincer, I.; Agelin-chaab, M.; Fraser, R.; Fowler, M. Thermal design and simulation of mini-channel cold plate for water cooled large sized prismatic lithium-ion battery. *Appl. Therm. Eng.* **2017**, *122*, 80–90.

33. Qian, Z.; Li, Y.; Rao, Z. Thermal performance of lithium-ion battery thermal management system by using mini-channel cooling. *Energy Convers. Manag.* **2016**, *126*, 622–631.

34. Chen, D.; Jiang, J.; Kim, G.; Yang, C.; Pesaran, A. Comparison of different cooling methods for lithium ion battery cells. *Appl. Therm. Eng.* **2016**, *94*, 846–854.

35. Hendricks, C.; Williard, N.; Mathew, S.; Pecht, M. A failure modes, mechanisms, and effects analysis (FMMEA) of lithium-ion batteries. *J. Power Sources* **2015**, *297*, 113–120.

36. Basu, S.; Hariharan, K.S.; Kolake, S.M.; Song, T.; Sohn, D.K.; Yeo, T. Coupled electrochemical thermal modelling of a novel Li-ion battery pack thermal management system. *Appl. Energy* **2016**, *181*, 1–13.

37. Hosseinzadeh, E.; Barai, A.; Marco, J.; Jennings, P. A Comparative Study on Different Cooling Strategies for Lithium-Ion Battery Cells. In Proceedings of the European Battery Hybrid and Fuel Cell Electric Vehicle Congress (EEVC 2017), Geneva, Switzerland, 14–16 March 2017; pp. 1–9.

38. XALT Energy. *XALT 53 Ah High Energy (HE) Superior Lithium Ion Cell MODEL F910-1001*; XALT Energy: Midland, MI, USA, 2016; pp. 1–2.

39. Gonser, B.W. *Modern Materials: Advances in Development and Applications*; Elsevier: Amsterdam, The Netherlands, 2013.

40. Zhang, S.; Vinson, M.; Beshenich, P.; Montesano, M. Evaluation and finite element modeling for new type of thermal material annealed pyrolytic graphite (APG). *Thermochim. Acta* **2006**, *442*, 6–9.

41. Thermacore. *Introduction to Aluminum and Magnesium Annealed Pyrolytic Graphite (k-Core)*; Thermacore: Lancaster, PA, USA, 2012.

42. Thermacore. k-Core®: A New Dimension in Conductive Heat Transfer. 2013. Available online: https://www.thermacore.com/documents/k-Core_Product_ Brochure.pdf (accessed on 15 May 2018).

43. Pittsburgh Corning. *FOAMGLAS® ONE*; Pittsburgh Corning: Pittsburgh, PA, USA, 2013.

44. Worwood, D.; Algoo, R.; McGlen, R.; Marco, J.; Greenwood, D. A study into different cell-level cooling strategies for cylindrical lithium-ion cells in automotive applications. *Int. J. Powertrains* **2018**, *7*, 199–266.

45. Kellner, Q.; Hosseinzadeh, E.; Chouchelamane, G.; Widanage, W.D.; Marco, J. Battery cycle life test development for high-performance electric vehicle applications. *J. Energy Storage* **2018**, *15*, 228–244.

46. Bergman, T.; Lavine, A.; Incropera, F.; Dewitt, D. *Fundamentals of Heat and Mass Transfer*; John Wiley & Sons: Chicago, IL, USA, 2011.

47. Onda, K.; Kameyama, H.; Hanamoto, T.; Ito, K. Experimental Study on Heat Generation Behavior of Small Lithium-Ion Secondary Batteries. *J. Electrochem. Soc.* **2003**, *150*, A285.

48. Xia, G.; Cao, L.; Bi, G. A review on battery thermal management in electric vehicle application. *J. Power Sources* **2017**, *367*, 90–105.

49. Sato, N. Thermal behavior analysis of lithium-ion batteries for electric and hybrid vehicles. *J. Power Sources* **2001**, *99*, 70–77.

50. Thomas, E.V.; Case, H.L.; Doughty, D.H.; Jungst, R.G.; Nagasubramanian, G.; Roth, E.P. Accelerated power degradation of Li-ion cells. *J. Power Sources* **2003**, *124*, 254–260.